Received: 14 February 2024 | Revised: 5 June 2024 | Accepted: 10 June 2024

DOI: 10.1002/nag.3797

RESEARCH ARTICLE

WILEY

Meshless method for wave propagation in poroelastic transversely isotropic half-space with the use of perfectly matched layer

Kamal Shaker | **Morteza Eskandari-Ghadi** | **Soheil Mohammadi**

School of Civil Engineering, College of Engineering, University of Tehran, Tehran, Iran

Correspondence
Morteza Eskandari-Ghadi, School of Civil Engineering, College of Engineering, University of Tehran, Tehran, Iran.
Email: ghadi@ut.ac.ir

Funding information
University of Tehran, Grant/Award Number: 27840/1/09

Abstract

Numerical investigation of wave propagation in transversely isotropic poroelastic half-space with the use of a new stretched coordinate system through the Meshless Local Petrov–Galerkin (MLPG) formulation is presented in this paper. To this end, the $\boldsymbol{u}-p$ formulation of Biot is adopted as the framework of the porous media. One approach to numerically solve the infinite domain problems is the use of an absorber layer in which the whole half-space is divided into two parts, that is (i) a finite part, in which the responses are interested, and (ii) the remaining semi-infinite part, which is replaced by a Perfectly Matched Layer (PML). The stretched coordinates in the PML are introduced in such a way that the wave propagating in it does not generate spurious reflection to the finite part. Comparing the numerical results with some existing exact solutions and evaluating the norm of error demonstrate that the response functions in the finite part are achievable as precise as desired. Some new results are also presented which show the validity of the numerical approach in poroelastic transversely isotropic domain.

KEYWORDS

MLPG, PML, soil-structure interaction, transversely porous media, wave propagation

1 | INTRODUCTION

The wave propagation problem in multiphysics, especially in saturated porous media, has been of great interest for both mathematicians and engineers due to its mathematical complexity and engineering applications. An accepted theory in this discipline is the Biot's theory,[1,2] which has been applied successfully by analytical and numerical approaches. Among different expressions of Biot's formulations for poroelastodynamic phenomena, which were proposed by considering some constrains and assumptions,[3–6] the formulation known as $\boldsymbol{u}-p$,[4] where $\boldsymbol{u}$ is the displacement vector and p is the pore fluid pressure, has been employed by many researchers due to its applicability, simplicity, and less unknown variables. In this formulation, the inertial effect due to the relative acceleration between solid and pore phases is neglected, which is precise enough in many engineering problems with low-frequency excitation.

During the last three decades, many researchers have concentrated on determining the responses of the poroelastic media with the use of Biot's theory and its simplified forms.[7–16] In the subject of elastodynamics of porous media, especially soil-structure-interaction, because of its nature the transversely isotropic properties for mechanical and hydraulic behavior are accepted. Vertical sedimentation and compaction over time are mainly the reasons for the transversely

isotropic behavior of the soil. Based on the $\boldsymbol{u} - p$ formulation of Biot's theory, the analytical solutions for the boundary value problems (BVPs) of transversely isotropic half-space with the use of the potential functions for decoupling of the coupled equations of motion and fluid continuity have been studied by Sahebkar and Eskandari–Ghadi.[10] Applying the stiffness method and the inverse Fourier transform, Ba et al.[17,18] solved the steady-state dynamic response of multilayered transversely isotropic half-space subjected to point forces and pore pressure. Dynamic responses of poroelastic layered media under transient and moving loads by means of integral transform techniques have been investigated in several works.[19–21] Furthermore, time history response of a half-space filled by transversely isotropic saturated materials subjected to obliquely incident seismic waves is studied in ref. 22.

Since performing both the analytical and semianalytical methods for various boundary conditions (BCs) and anisotropic property are complicated, the researchers have been forced to develop and implement numerical methods. The mathematical requirement for this problem is the concept of wave propagation in infinite domains.[23–25] Since imposing radiation condition in domain-based analysis, like finite element method (FEM), is not straightforward, applying numerical methods in wave propagation of unbounded domains needs special attention. To obviate the issue, several approaches have been proposed to make it possible to truncate the unbounded domain,[23,26–31] Absorbing boundary, proposed in refs. 26, 28, 29, is a successful numerical approach for these kinds of problems. In this method, the absorbing boundary, that is surrounding the truncated domain, is used to be replaced for the far-field points of the domain; meaning that the wave propagating toward the absorbing boundary is not reflecting back to the truncated domain as it is in real physics. However, Perfectly Matched Layer (PML), which was first introduced by Berenger in the context of electromagnetic waves,[32] is another innovation for numerical investigation for wave propagation of unbounded domain. The concept of PML in which the far-filed is replaced by a finite layer, was employed in electromagnetics and electrodynamics by some other researchers.[33,34] PML also has been used in elastic wave propagation in Cartesian, cylindrical, and spherical coordinate systems.[35–37] Chew et al.[34,35] with the use of the technique of PML obtained precise results for both time-harmonic and transient wave propagation in unbounded elastic media. Basu and Chopra[38,39] clearly explained the problem for one-dimensional wave propagation and extended it to three-dimensional case. Zeng and Liu[40] combined finite difference method with PML to study wave propagation in poroelastic material in the framework of $\boldsymbol{u} - \boldsymbol{u}$ formulation derived from the Biot's theory. Fathi et al.[41] proposed a hybrid formulation for elastic wave propagation in a heterogenous PML-truncated media in which displacement-stress and standard displacement formulations are respectively used for the PML and the interior domain. Zhang and Taciroglu[42] developed the standard PML to the viscoelastic PML that incorporates the Rayleigh damping mechanism. To remove the frequency singularity in transient elastic wave propagation, François et al.[43] proposed the complex-frequency-shifted PML in which a frequency shift is added to the stretching functions.

Computational modeling techniques have been employed to model and investigate the physical phenomena in engineering systems. These techniques require solving equations with partial derivatives that govern the physical phenomena. These partial differential equations can be analyzed using numerical methods such as finite element method, finite difference method, meshless method, and so forth. Some of these methods require discretization of the overall domain of the problem into elements, for example, FEM, and in some others like meshless methods, a set of nodes is used to represent the domain of interest. In fact, in the latter approach the relationship between the nodes defined in the domain does not generate elements. The meshless approach, which is used in this paper, generates a system of algebraic equations by using sparse nodes both on the boundary and inside the domain in order to derive the response to the excitation. Various meshless methods have been developed, including the Element Free Galerkin (EFG) method,[44] the Meshless Local Petrov–Galerkin (MLPG) method,[45] the Point Interpolation Method (PIM),[46] the Point Assembly Method (PAM),[46] the Finite Point Method (FPM),[47] and so forth. The MLPG method, presented in refs. 45, 48, is a meshless method in which the weak form equations are written over a set of local subdomains defined on the global domain, and no global background cells are required for integration.

On the other hand, to perform calculations on the weak form extracted by meshless methods, one may need to use some methods to generate shape functions, the most famous of which are the Smoothed Particle Hydrodynamics (SPH),[49,50] the Reproducing Kernel Particle Method (RKPM),[51,52] the Moving Least Squares (MLS),[44,53] the PIM,[46] the Radial Point Interpolation Method (RPIM).[52] Each of these methods of generating shape functions contains special features that distinguish their functions from each other. Some of these features are the partition of unity, the property of Kronecker's delta function, the linear field reproduction, stability, consistency, compatibility, and high flexibility to choose any arbitrary distribution of nodes on the boundary and inside the problem domain. In this paper, the Polynomial-Radial Point Interpolation Method (P-RPIM)[54] is used, in which the delta function property, high convergence, consistency (which is achieved by adding polynomial bases), and proper accuracy are its properties.

To enhance the accuracy of the approximate solutions obtained by the numerical methods, it is needed to know the effective sources may increase the errors for example, mesh/node distribution, field variable concentrations, singularities,

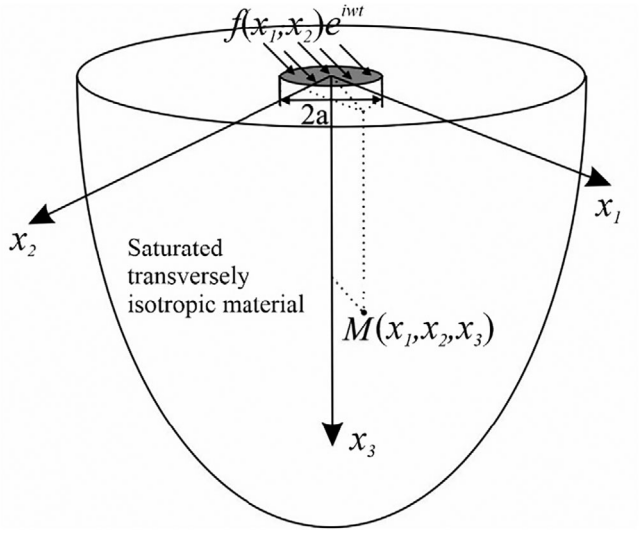

FIGURE 1 The half-space containing saturated transversely isotropic materials in both mechanical and hydraulic points of view subjected to arbitrary BCs. BCs, boundary conditions.

and jump conditions. The error analysis has been successfully performed to improve the efficiency and accuracy of the numerical methods. This analysis is done in two steps: (i) error estimation,[55–57] and (ii) geometry refinement based on the first step.[58–61] Besides, based on the estimated error, the refinement is generally done by two ways: (i) adding, moving, or remeshing/regenerating nodes (denoted as *h*-method), and (ii) using higher order interpolation function (so called *p*-method) to improve the accuracy. Also, simultaneous application of *h*- and *p*-methods is possible.

In this study, wave propagation due to an arbitrary time-harmonic finite surface excitation applied on a half-space containing saturated poroelastic transversely isotropic material in both mechanical and transport points of view is considered. The $\boldsymbol{u} - p$ formulation is adopted as the governing equations for the whole half-space. To the best knowledge of the authors, the PML based numerical investigation of wave propagation in unbounded anisotropic poroelastic domains has not been studied so far. To this end, defining a family of continuous stretched coordinate transformation to make PML, the equations of motion and their weak forms are written in the stretched coordinate system to obtain the local weak forms. In this regard, a family of transfer functions is used to make an image of the original problem in the stretched coordinate system. These transfer functions are proposed in such a way that the response functions in the new and old coordinate systems are the same in the finite region where the responses are desired (near field), and the wave energy is dissipated along the PML surrounding the near field. The parameters of the transfer functions are chosen in such a way that the outer boundary of the PML plays the role of the remote boundary.

To implement the MLPG method for estimation of nodal values, the P-RPIM is used to construct shape functions. The general form of the governing equations in the PML for the transversely isotropic saturated poroelastic material can be degenerated to some other problems such as: transversely isotropic elastic, isotropic elastic, and viscoelastic media. The procedure of the meshless implementation is summarized and two general forms of excitation, that is, stress wave propagation and forced vibration of a rigid foundation, are expressed. It is shown that the numerical results are collapsed on the analytical solutions in near field with high accuracy, while they are attenuated in the far-field.

2 | STATEMENT OF THE PROBLEM

Dynamic responses for a half-space containing transversely isotropic materials subjected to arbitrary BCs, such as forced vibration and stress vibration, in the frequency domain (as seen in Figure 1) are investigated by using a meshless approach. The mechanical and hydraulic properties of the half-space are considered transversely isotropic; meaning that the material properties in the depth direction are different from any direction in the planes perpendicular to the depth direction, and the material properties in any direction in this plane are the same. The governing equations of motion of this BVP are a special form of Biot's theory, known as the $\boldsymbol{u} - p$ formulation, in which the relative acceleration of the fluid and the solid skeleton is assumed to be negligible.

Due to the impossibility of manipulation with infinite/semi-infinite domains in domain-based numerical approaches, one can truncate the domain of the problem, and impose proper BCs around it in such way that the solutions in the truncated domain be equal to the corresponding region in the unbounded domain. To this end, a layer with a finite depth is defined around the finite domain denoted as near field, to be replaced for the surrounding unbounded domain namely far-field. This finite layer surrounding the near field, known as PML, absorbs the energy of the propagating waves in such a way that there will be no reflection to the near field. According to this definition, the infinite/semifinite domain can be divided into two separate regions: the near field and the far-field.

The near field is a part of the infinite/semifinite domain where the accuracy of the solutions of the problem is important, and the far-field is the rest of the domain where the accuracy and precision of the solution are not required. It is worth mentioning that in the far-field, the rate of attenuation of various functions and the smallness of the functions at the outer boundary of the PML are important. By replacing the entire infinite/semifinite medium with a near field and an absorbing layer around it, a solution can be reached that the functions in the near field are completely identical to the ones of the infinite/semifinite medium, and the absorbing layer plays the role of the rest of the infinite/semifinite medium. Thus, in this way the infinite/semi-infinite domain replaced by a finite domain and this modeling is suitable for numerical analysis of wave propagation problems.

In order to define this absorbent layer, it is necessary to write the governing equations in a new coordinate system, namely stretched coordinate system, which is an image of the physical coordinate system. This new coordinate system must be written in such a way that the response functions in the near field are equal to the original problem with appropriate accuracy. For numerical analysis of the problem, a meshless approach is used. In this method, a set/cloud of scattered nodes are chosen both in the domain and on its boundary, and the weak forms of the equations of motion are written using four degrees of freedom defined at each node, three of which are used for displacement vector $\boldsymbol{u}$ and one for fluid pressure p. Then, solving the obtained equations with the BCs, the nodal values at each node are calculated from which the stress tensor at every node in the domain is calculated by postprocessing analysis.

The numerical method used in this research is the MLPG method. It should be mentioned that the saturated porous medium is the general state, which with minor changes can be degenerated to dry homogeneous media, saturated porous homogeneous media, and dry homogeneous media.

3 | GOVERNING EQUATIONS IN THE STRETCHED COORDINATE SYSTEM

A saturated poroelastic material being transversely isotropic for both mechanical and hydraulic properties is considered, in such a way that the material axes of symmetry for both mechanical and flow of fluid are parallel. The governing equations of motion and Darci's law in the framework of $\boldsymbol{u} - p$ formulation, as a simplified version of Biot's formulation, where the relative pore fluid acceleration has been neglected, may be written in the form of[3,4]

$$\nabla \cdot \boldsymbol{\sigma} + \rho \boldsymbol{b} = \rho \ddot{\boldsymbol{u}} \tag{1a}$$

$$\dot{\mathbf{w}} = \frac{\boldsymbol{k}}{\eta}(-\nabla p + \rho^f \boldsymbol{b} - \rho^f \ddot{\boldsymbol{u}}) \tag{1b}$$

In Equation (1b), $\boldsymbol{\sigma}$ is the total Cauchy stress tensor, $\boldsymbol{u}$ is the displacement vector of solid skeleton, $\mathbf{w}$ and p are, respectively, the relative displacement vector of fluid with respect to the solid skeleton and the pore fluid pressure. In addition, $\boldsymbol{b}$ is the body force vector, and ρ^f, ρ^s and $\rho = (1-n)\rho_s + n\rho_f$ are the fluid, solid, and mixture mass densities, respectively, with n being the porosity. Furthermore, $\boldsymbol{k}$, which is a diagonal matrix with two independent eigenvalues for a transversely isotropic material, is intrinsic permeability tensor and eventually, η is dynamic viscosity of the fluid.

In the following, the stretched coordinate system is introduced, then the governing equations are written in this new coordinate system, and finally, the weak forms are obtained. The BCs involved in the problem are defined in the end of this section.

3.1 | Stretched coordinate system

The absorption layer formulation is one of the approaches used to replace a finite thickness layer for an infinite far-field. With this approach, the computational cost for domain-based numerical methods is greatly reduced. The energy of the advancing wave must be almost completely dissipated in this absorbent layer, and in this case, there will be no

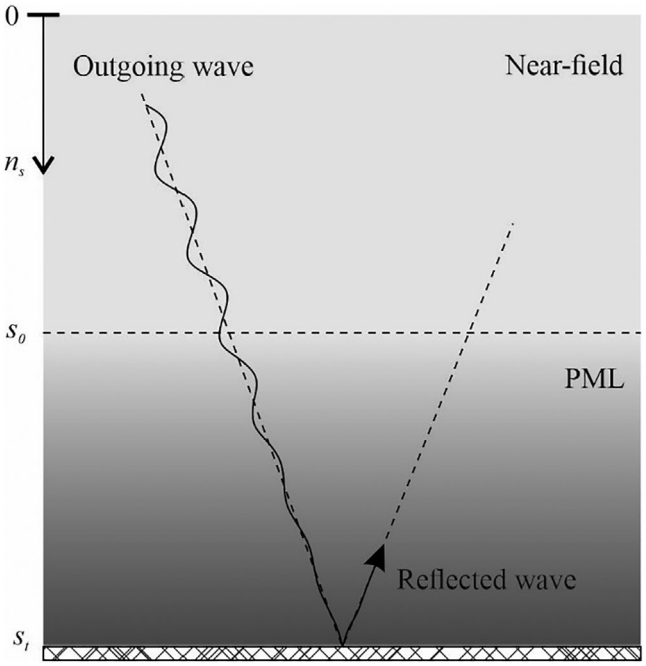

FIGURE 2 The near field adjacent to the PML. The propagated wave is attenuating in the PML, and so, there is no reflected wave propagating through the near field. PML, perfectly matched layer.

reflected wave from the end of the absorbent layer. Therefore, the numerical solution is performed in the near field with the highest accuracy. The response functions in the PML, which are affected by the attenuation procedure, are not correct. Nevertheless, the solution method followed in this approach does not affect the accuracy of the response functions in the near field. In this method, a frequency-dependent complex function, which is referred to as the transfer function from now on, is used to produce the standard formulation of the PML. This transfer function, which is used to image the far-field on the PML, initially defined by Chew and his colleagues.[62] If the coordinate system for the half-space is the physical coordinate system, the transfer function transfers the domain from the physical coordinate system to a new coordinate system which is called the stretched coordinate system. To define the equations in the stretched coordinate system, it is necessary to briefly discuss the requirements for the construction of the PML. As seen in Figure 2, there are two adjacent subdomains in the PML technique to define the whole domain of the problem:

- the near field where the responses are the same as the original problem,
- the PML around the near field, where the amplitude of any function is attenuating through and there is no reflection back to the near field.

Next, it is assumed that the attenuation of the wave amplitude takes place in the direction perpendicular to the interface of the near field and the PML. The coordinate variable normal to this common boundary is denoted by s. In this case, the near field and the PML are respectively defined in the intervals $0 < s < s_0$ and $s_0 < s < s_t$. Therefore, the thickness of the PML in the direction of n_s according to Figure 2 is $s_P = s_t - s_0$. The physical coordinate s inside the absorbent layer is depicted as $\tilde{s}$, and defined in the following form as a function of external excitation circular frequency ω, and λ_s, which is called stretching function:

$$\tilde{s} = \int_0^s \lambda_s(s',\ \omega)\mathrm{d}s' \tag{2}$$

It will be seen that $\tilde{s}$ has been considered as a function of both s and the frequency of the excitation for achieving the best accuracy. In classical studies conducted on the idea of the PML, the stretching function is chosen in the following form:

$$\lambda_s(s,\ \omega) = \alpha_s(s) + \frac{1}{i\omega}\beta_s(s) \tag{3}$$

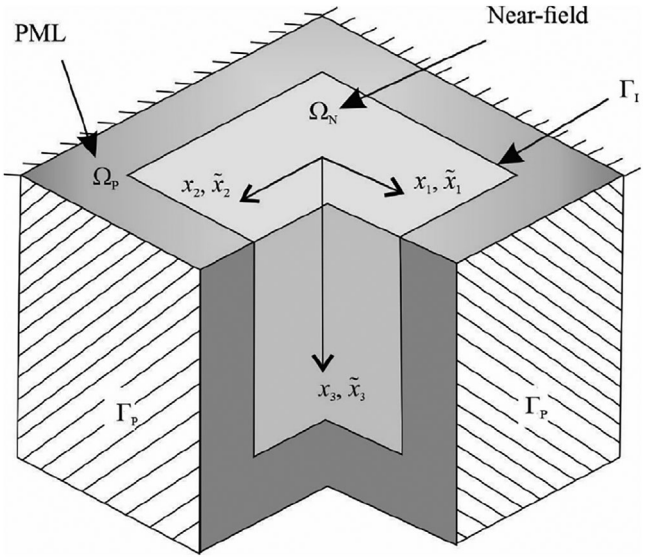

FIGURE 3 The near field and the PML in the stretched coordinate system. PML, perfectly matched layer.

so that $\alpha_s(s)$ is the scaling function which stretches or shortens the coordinate variable s, and $\beta_s(s)$ is the attenuation function reducing the amplitude of the propagating wave. In the evanescent wave, the term $\alpha_s(s)$ strengthens the action of reducing the wave amplitude by lengthening the real part of the coordinate variable s. Thus, $\alpha_s(s)$ is used to enhance the attenuation of the evanescent wave amplitude and $\beta_s(s)$ is used to enhance the attenuation of the propagating wave amplitude. For waves that consist of both types of waves, both functions must be defined appropriately. One of the limitations related to the definition of these two functions is that the wave does not break or refract when crossing the interface of the near field and the PML. In other words, the wave should not realize the interface when passing through this region. It is necessary and also sufficient that:

- $\alpha_s(0 \leqslant s \leqslant s_0) = 1$
- $\beta_s(0 \leqslant s \leqslant s_0) = 0$
- $\alpha_s(s)$ and $\beta_s(s)$ must be continuous, positive, and non-descending

in order to (i) have no reflected wave from the boundary between the near field and the PML when the wave is propagating through, (ii) have the responses in the near field to be as accurate as we wish, and (iii) the wave energy to be attenuated along the PML. To define the absorbing layer in order to attenuate the amplitude of the waves entering this area, the equations of motion and Darcy's law are written in the stretched complex coordinate system. In the frequency space, the variables of the stretched coordinate system are defined as follows:

$$\tilde{x}_i := \int_0^{x_i} \lambda_i(s, \omega) ds, \quad i = 1, 2, 3 \tag{4}$$

It should be noted that each of $\tilde{x}_i$ is assumed to be only a function of x_i. Equation (4) defines a new coordinate system in which the near field in the stretched and physical coordinate systems are exactly the same, while the positions on the outer boundaries of the PML are the interpretation of the remote points in the physical coordinate system. The transfer function λ_i and its parameters are used to speed up/down the attenuation of the response functions inside the PML along x_i-axis.

3.2 | Strong form of the equations in the stretched coordinate system

The coordinates x_i and the derivatives with respect to these coordinates in the equations of motion and the transport equation in the absorbing layer should be replaced by the stretched coordinate variables $\tilde{x}_i$ (see Figure 3):

$$\frac{\partial}{\partial \tilde{x}_i} = \frac{1}{\lambda_i(x_i)}\frac{\partial}{\partial x_i}, \qquad i = 1,\ 2,\ 3$$

$$\frac{\partial^2}{\partial \tilde{x}_i \partial \tilde{x}_j} = \frac{\partial}{\partial \tilde{x}_i}\left(\frac{1}{\lambda_j(x_j)}\frac{\partial}{\partial x_j}\right) = \frac{1}{\lambda_i(x_i)}\frac{\partial}{\partial x_i}\left(\frac{1}{\lambda_j(x_j)}\frac{\partial}{\partial x_j}\right)$$

$$= \begin{cases} \dfrac{-(\lambda_j(x_j))'}{(\lambda_j(x_j))^3}\dfrac{\partial}{\partial x_j} + \dfrac{1}{(\lambda_j(x_j))^2}\dfrac{\partial^2}{\partial x_j^2} & i = j \\ \dfrac{1}{\lambda_i(x_i)\lambda_j(x_j)}\dfrac{\partial^2}{\partial x_i \partial x_j} & i \neq j \end{cases} \tag{5}$$

in which the Einstein summation convention has not been used.

Before writing the equations in the stretched coordinate system, the equations are first transferred to the frequency space. In order to obtain the equations of motion for the poroelastic medium in the frequency space, it is sufficient to apply the Fourier transform which is defined as:

$$\hat{f}(\boldsymbol{x};\omega) = \int_{-\infty}^{+\infty} f(\boldsymbol{x};t)e^{-i\omega t}dt \tag{6}$$

for an integrable function in time domain $f(\boldsymbol{x};t)$. Thus, Equation (1) is written as:

$$\nabla \cdot \hat{\boldsymbol{\sigma}}(\boldsymbol{x};\omega) + \rho\hat{\boldsymbol{b}}(\boldsymbol{x};\omega) = \rho(i\omega)^2\hat{\boldsymbol{u}}(\boldsymbol{x};\omega) \tag{7a}$$

$$\nabla \cdot [(\rho^f k_{ij}(i\omega)^2 - \alpha_{ij}\eta(i\omega))\hat{u}_j(\boldsymbol{x};\omega) + k_{ij}\hat{p}_{,j}(\boldsymbol{x};\omega) - k_{ij}\rho^f\hat{b}_j(\boldsymbol{x};\omega)]\boldsymbol{e}_i - \frac{\eta}{M}(i\omega)\hat{p}(\boldsymbol{x};\omega) = 0 \tag{7b}$$

in frequency domain, where $\hat{\cdot}$ is the symbol of variables in frequency domain, and α_{ij} is Biot's effective stress tensor. The term ω in $(\boldsymbol{x};\omega)$ is dropped from now on for simplicity. Equation (7b), in the stretched coordinate system, is rewritten as follows:

$$\frac{\hat{\sigma}_{ij}(\tilde{\boldsymbol{x}})}{\partial \tilde{x}_i} + \rho\hat{b}_j(\tilde{\boldsymbol{x}}) = \rho(i\omega)^2\hat{u}_j(\tilde{\boldsymbol{x}}), \quad j = 1,2,3 \tag{8}$$

Using (5) in (8), the equations are transferred to the physical coordinate system:

$$\frac{1}{\lambda_1}\frac{\hat{\sigma}_{1j}(\boldsymbol{x})}{\partial x_1} + \frac{1}{\lambda_2}\frac{\hat{\sigma}_{2j}(\boldsymbol{x})}{\partial x_2} + \frac{1}{\lambda_3}\frac{\hat{\sigma}_{3j}(\boldsymbol{x})}{\partial x_3} + \rho\hat{b}_j(\boldsymbol{x}) = \rho(i\omega)^2\hat{u}_j(\boldsymbol{x}), \quad j = 1,2,3 \tag{9}$$

multiplying both sides of these equations by $\lambda_1\lambda_2\lambda_3$, yields:

$$\nabla \cdot (\hat{\boldsymbol{\sigma}}^T(\boldsymbol{x})\boldsymbol{\Lambda}(\boldsymbol{x})) + \rho\lambda_1(\boldsymbol{x})\lambda_2(\boldsymbol{x})\lambda_3(\boldsymbol{x})\hat{\boldsymbol{b}}(\boldsymbol{x}) = \rho(i\omega)^2\lambda_1(\boldsymbol{x})\lambda_2(\boldsymbol{x})\lambda_3(\boldsymbol{x})\hat{\boldsymbol{u}}(\boldsymbol{x}) \tag{10}$$

in which $\boldsymbol{\Lambda}$ with the use of (3) is written as:

$$\boldsymbol{\Lambda} = \begin{bmatrix} \lambda_2\lambda_3 & 0 & 0 \\ 0 & \lambda_1\lambda_3 & 0 \\ 0 & 0 & \lambda_1\lambda_2 \end{bmatrix} = \begin{bmatrix} \alpha_2^s\alpha_3^s & 0 & 0 \\ 0 & \alpha_1^s\alpha_3^s & 0 \\ 0 & 0 & \alpha_1^s\alpha_2^s \end{bmatrix}$$
$$+\frac{1}{i\omega}\begin{bmatrix} \alpha_2^s\beta_3^s + \alpha_3^s\beta_2^s & 0 & 0 \\ 0 & \alpha_1^s\beta_3^s + \alpha_3^s\beta_1^s & 0 \\ 0 & 0 & \alpha_2^s\beta_1^s + \alpha_1^s\beta_2^s \end{bmatrix}$$
$$\frac{1}{(i\omega)^2}\begin{bmatrix} \beta_2^s\beta_3^s & 0 & 0 \\ 0 & \beta_1^s\beta_3^s & 0 \\ 0 & 0 & \beta_1^s\beta_2^s \end{bmatrix} = \boldsymbol{\Lambda}_e + \frac{1}{i\omega}\boldsymbol{\Lambda}_p + \frac{1}{(i\omega)^2}\boldsymbol{\Lambda}_\omega \tag{11}$$

Considering the properties of the scaling and attenuation functions, one may select $\boldsymbol{\Lambda}_p = \boldsymbol{\Lambda}_\omega = 0$ and $\boldsymbol{\Lambda}_e = \delta_{ij}$ in the near field. On the other hand, substituting (11) in (10) results in

$$\begin{aligned}&\nabla \cdot \left(\hat{\boldsymbol{\sigma}}^T(\boldsymbol{x})\boldsymbol{\Lambda}_e + \frac{1}{i\omega}\hat{\boldsymbol{\sigma}}^T(\boldsymbol{x})\boldsymbol{\Lambda}_p + \frac{1}{(i\omega)^2}\hat{\boldsymbol{\sigma}}^T(\boldsymbol{x})\boldsymbol{\Lambda}_\omega \right) + \rho \left(\bar{a}_1 + \frac{1}{i\omega}\bar{a}_2 + \frac{1}{(i\omega)^2}\bar{a}_3 + \frac{\bar{a}_3}{(i\omega)^3} \right) \hat{\boldsymbol{b}}(\boldsymbol{x}) \\ &= \rho \left((i\omega)^2 \bar{a}_1 + i\omega \bar{a}_2 + \bar{a}_3 + \frac{\bar{a}_3}{i\omega} \right) \hat{\boldsymbol{u}}(\boldsymbol{x})\end{aligned} \tag{12}$$

in which

$$\begin{aligned}&\bar{a}_1 = \alpha_1^s \alpha_2^s \alpha_3^s, \bar{a}_2 = \alpha_1^s \alpha_2^s \beta_3^s + \alpha_1^s \beta_2^s \alpha_3^s + \beta_1^s \alpha_2^s \alpha_3^s, \\ &\bar{a}_3 = \alpha_1^s \beta_2^s \beta_3^s + \beta_1^s \beta_2^s \alpha_3^s + \beta_1^s \alpha_2^s \beta_3^s, \bar{a}_4 = \beta_1^s \beta_2^s \beta_3^s\end{aligned} \tag{13}$$

with the same procedure, one may write the Equation (7b) as:

$$\left(\rho^f k_{ij} (i\omega)^2 - \alpha_{ij} \eta (i\omega) \right) \frac{\partial \hat{u}_j(\boldsymbol{x})}{\partial x_k} \frac{\partial x_k}{\partial \tilde{x}_i} + k_{ij} \frac{\partial}{\partial x_k} \left(\frac{\partial \hat{p}(\boldsymbol{x})}{\partial x_l} \frac{\partial x_l}{\partial \tilde{x}_j} \right) \frac{\partial x_k}{\partial \tilde{x}_i} - k_{ij} \rho^f \frac{\partial \hat{b}_j(\boldsymbol{x})}{\partial x_k} \frac{\partial x_k}{\partial \tilde{x}_i} - \frac{\eta}{M} (i\omega) \hat{p}(\boldsymbol{x}) = 0 \tag{14}$$

It is known that permeability tensor and Biot's effective stress tensor are diagonal with two distinct eigen values and two perpendicular eigen vectors, one of which is in x_3-direction and the other is any vector in x_3-plane. Therefore, one may write (14) as

$$\begin{aligned}&\left(\rho^f k_{11} (i\omega)^2 - \alpha_{11} \eta (i\omega) \right) \Lambda_{11} \frac{\partial \hat{u}_1(\boldsymbol{x})}{\partial x_1} + \left(\rho^f k_{22} (i\omega)^2 - \alpha_{22} \eta (i\omega) \right) \Lambda_{22} \frac{\partial \hat{u}_2(\boldsymbol{x})}{\partial x_2} \\ &+ \left(\rho^f k_{33} (i\omega)^2 - \alpha_{33} \eta (i\omega) \right) \Lambda_{33} \frac{\partial \hat{u}_3(\boldsymbol{x})}{\partial x_3} + k_{11} \frac{\partial}{\partial x_1} \left(\frac{\partial \hat{p}(\boldsymbol{x})}{\partial x_1} \Theta_{11} \right) + k_{22} \frac{\partial}{\partial x_2} \left(\frac{\partial \hat{p}(\boldsymbol{x})}{\partial x_2} \Theta_{22} \right) \\ &+ k_{33} \frac{\partial}{\partial x_3} \left(\frac{\partial \hat{p}(\boldsymbol{x})}{\partial x_3} \Theta_{33} \right) - k_{11} \rho^f \Lambda_{11} \frac{\partial \hat{b}_1(\boldsymbol{x})}{\partial x_1} - k_{22} \rho^f \Lambda_{22} \frac{\partial \hat{b}_2(\boldsymbol{x})}{\partial x_2} - k_{33} \rho^f \Lambda_{33} \frac{\partial \hat{b}_3(\boldsymbol{x})}{\partial x_3} \\ &- \frac{\eta}{M} (i\omega) \lambda_1 \lambda_2 \lambda_3 \hat{p}(\boldsymbol{x}) = 0\end{aligned} \tag{15}$$

in which $\boldsymbol{\Theta}$ is:

$$\boldsymbol{\Theta} = \begin{bmatrix} \frac{\lambda_2 \lambda_3}{\lambda_1} & 0 & 0 \\ 0 & \frac{\lambda_1 \lambda_3}{\lambda_2} & 0 \\ 0 & 0 & \frac{\lambda_1 \lambda_2}{\lambda_3} \end{bmatrix} \tag{16}$$

Since $\Lambda_{11,}$ Λ_{22} and Λ_{33} are respectively independent of $x_{1,}$ x_2 and $x_{3,}$ and since $\boldsymbol{k}$ and $\boldsymbol{\alpha}$ are fixed tensors, one can write:

$$\begin{aligned}&\frac{\partial}{\partial x_1} \left[(\rho^f k_{11} (i\omega)^2 - \alpha_{11} \eta (i\omega)) \Lambda_{11} \hat{u}_1(\boldsymbol{x}) \right] + \frac{\partial}{\partial x_2} \left[(\rho^f k_{22} (i\omega)^2 - \alpha_{22} \eta (i\omega)) \Lambda_{22} \hat{u}_2(\boldsymbol{x}) \right] \\ &+ \frac{\partial}{\partial x_3} \left[(\rho^f k_{33} (i\omega)^2 - \alpha_{33} \eta (i\omega)) \Lambda_{33} \hat{u}_3(\boldsymbol{x}) \right] + \frac{\partial}{\partial x_1} \left[k_{11} \frac{\partial \hat{p}(\boldsymbol{x})}{\partial x_1} \Theta_{11} \right] + \frac{\partial}{\partial x_2} \left[k_{22} \frac{\partial \hat{p}(\boldsymbol{x})}{\partial x_2} \Theta_{22} \right] \\ &+ \frac{\partial}{\partial x_3} \left[k_{33} \frac{\partial \hat{p}(\boldsymbol{x})}{\partial x_3} \Theta_{33} \right] - \frac{\partial}{\partial x_1} \left[k_{11} \rho^f \Lambda_{11} \hat{b}_1(\boldsymbol{x}) \right] - \frac{\partial}{\partial x_2} \left[k_{22} \rho^f \Lambda_{22} \hat{b}_2(\boldsymbol{x}) \right] - \frac{\partial}{\partial x_3} \left[k_{33} \rho^f \Lambda_{33} \hat{b}_3(\boldsymbol{x}) \right] \\ &- \frac{\eta}{M} (i\omega) \lambda_1 \lambda_2 \lambda_3 \hat{p}(\boldsymbol{x}) = 0\end{aligned} \tag{17}$$

In vector space, the above equation is expressed as:

$$\nabla \cdot \left[(\rho^f k_{ij} (i\omega)^2 - \alpha_{ij} \eta (i\omega)) \Lambda_{jk} \hat{u}_k(\boldsymbol{x}) + k_{ij} \Theta_{jk} \hat{p}_{,k}(\boldsymbol{x}) - k_{ij} \rho^f \Lambda_{jk} \hat{b}_k(\boldsymbol{x}) \right] \boldsymbol{e}_i - \frac{\eta}{M} (i\omega) \lambda_1 \lambda_2 \lambda_3 \hat{p}(\boldsymbol{x}) = 0 \tag{18}$$

Consequently, the governing Equations (14) and (18) are used in the remaining of this study to establish the required procedure for numerical solution.

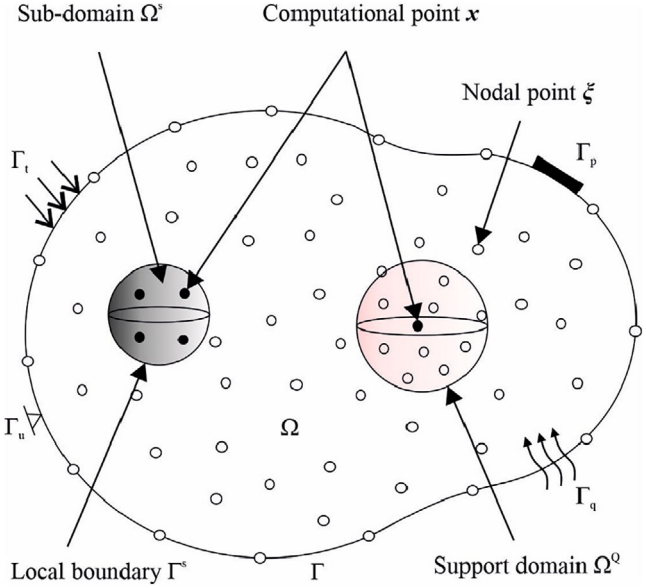

FIGURE 4 Ω^s and Γ^s are the local subdomain and its boundary, which are used for the weak form integration. The support domain Ω^Q corresponding to the computational point $\boldsymbol{x}$ is used for constructing the shape functions. Different BCs are also shown. BCs, boundary conditions.

3.3 | Weak form of the equations in the stretched coordinate system

In order to obtain the weak form of the governing equations, the divergence theorem is used after integrating the inner product of the strong form Equations (14) and (18) with the arbitrary weight vector $\boldsymbol{w}^T = \{w_1, w_2, w_3\}$ and arbitrary weight function w_p, respectively, over every subset of the global domain (called local subdomain):

$$\int_{\Gamma^s} \boldsymbol{w} \cdot (\hat{\boldsymbol{\sigma}}^T(\boldsymbol{x})\boldsymbol{\Lambda} \cdot \boldsymbol{n}) d\Gamma - \int_{\Omega^s} \nabla \boldsymbol{w} : (\hat{\boldsymbol{\sigma}}^T(\boldsymbol{x})\boldsymbol{\Lambda}) d\Omega + \int_{\Omega^s} \boldsymbol{w} \cdot (\rho\lambda_1\lambda_2\lambda_3 \hat{\boldsymbol{b}}(\boldsymbol{x}) - \rho(i\omega)^2 \lambda_1\lambda_2\lambda_3 \hat{\boldsymbol{u}}(\boldsymbol{x})) d\Omega = 0 \tag{19}$$

and

$$\begin{aligned} &\int_{\Gamma^s} w_p[(\rho^f \boldsymbol{k}(i\omega)^2 - \boldsymbol{\alpha}\eta(i\omega))\boldsymbol{\Lambda}\hat{\boldsymbol{u}}(\boldsymbol{x}) + \boldsymbol{k}\Theta\nabla\hat{p}(\boldsymbol{x}) - \rho^f \boldsymbol{k}\Lambda\hat{b}(\boldsymbol{x})] \cdot \boldsymbol{n} d\Gamma \\ &- \int_{\Omega^s} (\nabla w_p)^T \cdot [(\rho^f \boldsymbol{k}(i\omega)^2 - \boldsymbol{\alpha}\eta(i\omega))\boldsymbol{\Lambda}\hat{\boldsymbol{u}}(\boldsymbol{x}) + \boldsymbol{k}\Theta\nabla\hat{p}(\boldsymbol{x}) - \rho^f \boldsymbol{k}\Lambda\hat{b}(\boldsymbol{x})] d\Omega \\ &- \int_{\Omega^s} \frac{i\omega\eta}{M} w_p \lambda_1\lambda_2\lambda_3 \hat{p}(\boldsymbol{x}) d\Omega = 0 \end{aligned} \tag{20}$$

in which Ω^s represents the local subdomain inside the global domain Ω, and Γ^s is its boundary (see Figure 4 for the global domain and the local subdomain). The weak forms for the near field in the physical and stretched coordinate systems are the same.

On the other hand, the total stress can be decomposed into effective stress on solid particles and fluid pressure as Biot introduced:

$$\hat{\boldsymbol{\sigma}}(\boldsymbol{x}) = \hat{\boldsymbol{\sigma}}^s(\boldsymbol{x}) - \hat{p}(\boldsymbol{x})\boldsymbol{\alpha} \tag{21}$$

In this equation, $\hat{\boldsymbol{\sigma}}^s(\boldsymbol{x}) = \hat{\boldsymbol{\sigma}}''(\boldsymbol{x})$ ($\hat{\boldsymbol{\sigma}}''(\boldsymbol{x})$ is the Biot's effective stress. Substituting (21) in (19) leads to:

$$\begin{aligned} &\int_{\Gamma^s} \boldsymbol{w} \cdot ((\hat{\boldsymbol{\sigma}}^s(\boldsymbol{x}))^T \boldsymbol{\Lambda} - \hat{p}(\boldsymbol{x})\boldsymbol{\alpha}\Lambda) \cdot \boldsymbol{n} d\Gamma - \int_{\Omega^s} \nabla \boldsymbol{w} : ((\hat{\boldsymbol{\sigma}}^s(\boldsymbol{x}))^T \boldsymbol{\Lambda} - \hat{p}(\boldsymbol{x})\boldsymbol{\alpha}\Lambda) d\Omega \\ &+ \int_{\Omega^s} \boldsymbol{w} \cdot (\rho\lambda_1\lambda_2\lambda_3 \hat{\boldsymbol{b}}(\boldsymbol{x}) - \rho(i\omega)^2 \lambda_1\lambda_2\lambda_3 \hat{\boldsymbol{u}}(\boldsymbol{x})) d\Omega = 0 \end{aligned} \tag{22}$$

In these weak form equations, there are some integral terms defined on the boundaries of the local subdomains. According to the location of each subdomain, its appropriate BCs are defined.

3.4 | Definition of BCs

In the previous section, the weak form Equations (19) and (20) have been written on the local subdomains. The number of degrees of freedom of each node is four. Also, in order to increase the accuracy of the solutions, the local subdomains should have a suitable dispersion in the whole domain. Then, appropriate BCs should be defined and applied on each of these subdomains. It is known that the displacement and stress BCs are coupled; however, they are independent from the pore fluid pressure and hydraulic flux BCs. Thus, the boundary of the local subdomain is divided into the following subsets:

- Γ_u: on which the displacements are known,
- Γ_t: on which the stresses are known,
- $\Gamma_{ut} = \Gamma_{tu}$: on which some components of the stress tensor and some other components of the displacement vector are known. If $\boldsymbol{n}$, $\boldsymbol{t}$, and $\boldsymbol{u}$ be the unit normal vector to the surface, the traction vector and the displacement on the surface, respectively, then two conditions are considerable:
  1. $\boldsymbol{t}_n = \boldsymbol{t} \cdot \boldsymbol{n}$ is known and $\boldsymbol{t}_t = \boldsymbol{t} - \boldsymbol{t} \cdot \boldsymbol{n}$ is unknown. So, $\boldsymbol{u}_t = \boldsymbol{u} - \boldsymbol{u} \cdot \boldsymbol{n}$ is known.
  2. $\boldsymbol{t}_t = \boldsymbol{t} - \boldsymbol{t} \cdot \boldsymbol{n}$ is known and $\boldsymbol{t}_n = \boldsymbol{t} \cdot \boldsymbol{n}$ is unknown. So, $\boldsymbol{u}_n = \boldsymbol{u} \cdot \boldsymbol{n}$ is known.

  Thus, the whole boundary may be shown as $\Gamma = \Gamma_u \cup \Gamma_t \cup \Gamma_{u_t t_n} \cup \Gamma_{u_n t_t}$ in which Γ_u, Γ_t, $\Gamma_{u_t t_n}$ and $\Gamma_{u_n t_t}$ are disjoint sets. For the BCs related to p and $\boldsymbol{q}$ there are:

- Γ_p: on which the pressure is known.
- Γ_q: on which the fluid flow is known.

  Thus, $\Gamma = \Gamma_p \cup \Gamma_q$.
  In general, the combination of these two sets of BCs can be experienced by the surface of the sub-domains

$$\Gamma^s = \Gamma_i^s \cup \Gamma_{up}^s \cup \Gamma_{uq}^s \cup \Gamma_{tp}^s \cup \Gamma_{tq}^s \cup \Gamma_{u_t t_n p}^s \cup \Gamma_{u_t t_n q}^s \cup \Gamma_{u_n t_t p}^s \cup \Gamma_{u_n t_t q}^s \tag{23}$$

where Γ_i^s is the boundary of the local subdomain which does not coincide with any previously defined BCs (embraced in the global domain). Note that, in the regions where the local subdomain does not share a surface with the boundary of the problem domain, the condition is $\Gamma^s = \Gamma_i^s$.

Therefore, in the most comprehensive form, the BCs are summarized as follows:

$$\begin{aligned}
&\boldsymbol{u} = \boldsymbol{u}^\circ \text{ and } p = p^\circ \text{ on } \Gamma_{up}^s \\
&\boldsymbol{u} = \boldsymbol{u}^\circ \text{ and } \boldsymbol{q} = \boldsymbol{q}^\circ \text{ on } \Gamma_{uq}^s \\
&\boldsymbol{t} = \boldsymbol{t}^\circ \text{ and } p = p^\circ \text{ on } \Gamma_{tp}^s \\
&\boldsymbol{t} = \boldsymbol{t}^\circ \text{ and } \boldsymbol{q} = \boldsymbol{q}^\circ \text{ on } \Gamma_{tq}^s \\
&\boldsymbol{u}_t = \boldsymbol{u}_t^\circ, \boldsymbol{t}_n = \boldsymbol{t}_n^\circ, \text{ and } p = p^\circ \text{ on } \Gamma_{u_t t_n p}^s \\
&\boldsymbol{u}_n = \boldsymbol{u}_n^\circ, \boldsymbol{t}_t = \boldsymbol{t}_t^\circ, \text{ and } p = p^\circ \text{ on } \Gamma_{u_n t_t p}^s \\
&\boldsymbol{u}_t = \boldsymbol{u}_t^\circ, \boldsymbol{t}_n = \boldsymbol{t}_n^\circ, \text{ and } \boldsymbol{q} = \boldsymbol{q}^\circ \text{ on } \Gamma_{u_t t_n q}^s \\
&\boldsymbol{u}_n = \boldsymbol{u}_n^\circ, \boldsymbol{t}_t = \boldsymbol{t}_t^\circ, \text{ and } \boldsymbol{q} = \boldsymbol{q}^\circ \text{ on } \Gamma_{u_n t_t q}^s
\end{aligned} \tag{24}$$

in which the terms $.^\circ$ are known functions on a subset of the boundary.

4 | MLPG METHOD

In the last two decades, meshless approaches due to the compatibility, construction of approximate solution in terms of nodal values without the requirement of connectivity information, the flexibility in adding/deleting nodes, ease of the

treatment of discontinuities, and large deformation, have been regarded for the numerical analysis of various problems in continuum mechanics. Meshless methods have been developed to establish the system of algebraic equations over the domain on interest without generating or using elements. In these methods, the collection of scattered nodes on the entire domain and its boundary is used to express (not discretize) the domain of the problem and its boundary. Since these nodes do not form any element, information about the relationship between the nodes in the form of the relationship that is involved in element-based methods is not required.

As mentioned before, various expressions of meshless methods have been presented so far, each of which has specific characteristics and assumptions.[44,48] Many of these methods use the weak form formulation on the global domain or on the subsets of the whole domain as subdomains. In the formulation defined over the global domain, background cells are usually required for the weak form integration. So, these methods cannot be called completely meshless. Alternatively, the methods that use the local subdomains may not need the global generation of cells. In this paper, MLPG method is used for creating the required equations.

In meshless approaches, each of the shape function generation methods may have specific features, which are the partition of unity, the property of Kronecker's delta function, the linear field reproduction, stability, consistency, compatibility, and the flexibility in choosing the distribution of nodes inside the domain and its boundary. The more the features satisfied by the method the more the accurate numerical results achieve. In FEM, the shape functions are generated based on the elements, and the calculations related to the shape functions are easily performed. On the other hand, the construction of shape functions in meshless methods has certain complications. For instance, in some meshless methods, contrary to FEM, the property of Kronecker's delta function does not exist.

There are various methods for constructing shape functions among them one can mention SPH,[49,50] RKPM,[51,52] MLS,[44,53] PIM,[46] RPIM.[52] The shape functions constructed by the RPIM are not consistent. But there is no severe concern in the regard of convergency for continuous function approximations.[63] To escape from inconsistency of the shape functions, polynomial basis functions can be added to the radial basis functions in the RPIM method.[54] Furthermore, by adding the polynomial basis functions to the radial basis functions, the accuracy dependence of the numerical results on the shape function parameters in the RPIM method is significantly reduced. The P-RPIM method, which is presented in the following subsection, is used to generate shape functions.

4.1 | P-RPIM for generation of the shape functions

In this section, the process of constructing shape functions using the P-RPIM is described briefly. Suppose Ω^Q is the support domain corresponding to the computing point $\boldsymbol{x} = (x_1, x_2, x_3)$. This area is used to estimate the response functions at $\boldsymbol{x}$ (see Figure 4). To interpolate/extrapolate the approximation function v in the support domain Ω^Q, n nodal points

$$\boldsymbol{\xi} = \{\boldsymbol{\xi}^1, \boldsymbol{\xi}^2, \dots, \boldsymbol{\xi}^n\}, \boldsymbol{\xi}^i = (x_1, x_2, x_3), i = 1, 2, \dots, n, \tag{25}$$

which are selected based on a suitable distribution, are used. The estimated function under the condition

$$\sum_{j=1}^{n} P_k(\boldsymbol{\xi}_j) a_j = 0, \ 1 \le k \le m \tag{26}$$

is equal to:

$$v^h(\boldsymbol{x}) = \sum_{k=1}^{n} R_k(\boldsymbol{x}, \boldsymbol{\xi}) a_k + \sum_{j=1}^{m} P_j(\boldsymbol{x}) b_j = \boldsymbol{R}(\boldsymbol{x}, \boldsymbol{\xi})\boldsymbol{a} + \boldsymbol{P}(\boldsymbol{x})\boldsymbol{b} \tag{27}$$

where R_k and P_j are, respectively, the radial and the polynomial basis functions. The condition (26) guarantees the independence of the polynomial basis functions from the radial ones and thus results in some unique values for $\boldsymbol{a}$ and $\boldsymbol{b}$. The set of radial basis functions inside Ω^Q centered at $\boldsymbol{x}$ is equal to:

$$\boldsymbol{R}(\boldsymbol{x}, \boldsymbol{\xi}) = \{R(\boldsymbol{x}, \boldsymbol{\xi}_1), R(\boldsymbol{x}, \boldsymbol{\xi}_2), \dots, R(\boldsymbol{x}, \boldsymbol{\xi}_n)\} \tag{28}$$

$\boldsymbol{a} = \{a_1, a_2, \dots, a_n\}$ is the vector of unknown coefficients related to radial basis functions. Also, the set of polynomial basis functions inside Ω^Q is in the form

$$\boldsymbol{P}(\boldsymbol{x}) = \{P_1(\boldsymbol{x}), P_2(\boldsymbol{x}), \dots, P_m(\boldsymbol{x})\} \tag{29}$$

and $\boldsymbol{b} = \{b_1, b_2, \dots, b_m\}$ is the unknown coefficients associated with it. Considering n nodal values $\widehat{\boldsymbol{\upsilon}} = \{\widehat{\upsilon}_1, \widehat{\upsilon}_2, \dots, \widehat{\upsilon}_n\}$ in Ω^Q, the set of linear Equations (26) and (27) are written in the following form:

$$\boldsymbol{R}_Q\boldsymbol{a} + \boldsymbol{P}_Q\boldsymbol{b} = \widehat{\boldsymbol{\upsilon}}, \boldsymbol{P}_Q^T\boldsymbol{a} = 0 \tag{30}$$

where

$$\boldsymbol{R}_Q = \begin{bmatrix} R(\xi_1,\xi_1) & R(\xi_1,\xi_2) & \dots & R(\xi_1,\xi_n) \\ R(\xi_2,\xi_1) & R(\xi_2,\xi_2) & \dots & R(\xi_2,\xi_n) \\ . & . & \dots & . \\ . & . & \dots & . \\ R(\xi_n,\xi_1) & R(\xi_n,\xi_2) & \dots & R(\xi_n,\xi_n) \end{bmatrix} \tag{31}$$

$$\boldsymbol{P}_Q = \begin{bmatrix} P_1(\xi_1) & P_2(\xi_1) & \dots & P_m(\xi_1) \\ P_1(\xi_2) & P_2(\xi_2) & \dots & P_m(\xi_2) \\ . & . & \dots & . \\ . & . & \dots & . \\ P_1(\xi_n) & P_2(\xi_n) & \dots & P_m(\xi_n) \end{bmatrix} \tag{32}$$

Solving (30) for the unknown coefficient vectors $\boldsymbol{a}$ and $\boldsymbol{b}$ yields

$$\boldsymbol{a} = \boldsymbol{S}_a\widehat{\boldsymbol{\upsilon}}, \boldsymbol{b} = \boldsymbol{S}_b\widehat{\boldsymbol{\upsilon}} \tag{33}$$

in which

$$\boldsymbol{S}_a = \boldsymbol{R}_Q^{-1}\left[\boldsymbol{I} - \boldsymbol{P}_Q\left(\boldsymbol{P}_Q^T\boldsymbol{R}_Q\boldsymbol{P}_Q\right)^{-1}\boldsymbol{P}_Q^T\boldsymbol{R}_Q^{-1}\right], \quad \boldsymbol{S}_b = \left(\boldsymbol{P}_Q^T\boldsymbol{R}_Q\boldsymbol{P}_Q\right)^{-1}\boldsymbol{P}_Q^T\boldsymbol{R}_Q^{-1}, \tag{34}$$

and $\boldsymbol{I}$ is the unit diagonal matrix. Substituting $\boldsymbol{a}$ and $\boldsymbol{b}$ in (27), the approximation of the desired function is obtained in terms of the nodal values:

$$\upsilon^h(\boldsymbol{x}) = \sum_{k=1}^{n}\varphi_k(\boldsymbol{x},\boldsymbol{\xi})\widehat{\upsilon}^k = \boldsymbol{\varphi}(\boldsymbol{x},\boldsymbol{\xi})\,\widehat{\boldsymbol{\upsilon}} \tag{35}$$

so that the vector of shape functions is written as:

$$\boldsymbol{\varphi}(\boldsymbol{x},\boldsymbol{\xi}) = \boldsymbol{R}(\boldsymbol{x},\boldsymbol{\xi})\boldsymbol{S}_a + \boldsymbol{P}(\boldsymbol{x})\boldsymbol{S}_b = \{\varphi_1(\boldsymbol{x},\boldsymbol{\xi}), \varphi_2(\boldsymbol{x},\boldsymbol{\xi}), \dots, \varphi_n(\boldsymbol{x},\boldsymbol{\xi})\} \tag{36}$$

Thus, n shape functions are obtained from Equation (36) to estimate $\upsilon^h(\boldsymbol{x})$. In addition to the approximation function (35), the derivative of that is calculated as:

$$\upsilon^h_{,i}(\boldsymbol{x}) = \sum_{k=1}^{n}\varphi_{k,i}(\boldsymbol{x},\boldsymbol{\xi})\widehat{\upsilon}^k = \boldsymbol{\varphi}_{,i}(\boldsymbol{x},\boldsymbol{\xi})\widehat{\boldsymbol{\upsilon}} \tag{37}$$

where

$$\varphi_{k,l}(\boldsymbol{x},\boldsymbol{\xi}) = \sum_{i=1}^{n}\frac{\partial R_i(\boldsymbol{x},\boldsymbol{\xi})}{\partial x_l}\boldsymbol{S}^a_{ik} + \sum_{j=1}^{m}\frac{\partial P_j(\boldsymbol{x})}{\partial x_l}\boldsymbol{S}^b_{jk} \tag{38}$$

In the three-dimensional problem, the shape functions may be assumed to be the same in all three directions, in which the shape functions in each direction are obtained using (36).

4.2 | Discretized equations in the stretched coordinate system

The weak forms of the governing equations in the stretched coordinate system have been given as Equations (19) and (20) in Section 3.3. All terms in these equations are in tensor form. To easily manipulate with these terms, they should be rewritten in matrix form (see Appendix A for more details). Inserting (A.1–A.16) from Appendix A in Equations (19) and (20) results in:

$$\begin{aligned}
&\int_{\Gamma^s} \boldsymbol{w}(\boldsymbol{x})\bar{\boldsymbol{N}}(\boldsymbol{x})\boldsymbol{C}\bar{B}(\boldsymbol{x})\widehat{\hat{\boldsymbol{u}}}d\Gamma - \int_{\Gamma^s} \boldsymbol{w}(\boldsymbol{x})\bar{\boldsymbol{N}}(\boldsymbol{x})\bar{\boldsymbol{\alpha}}\varphi(\boldsymbol{x})\widehat{\hat{\boldsymbol{p}}}d\Gamma \\
&- \int_{\Omega^s} (\boldsymbol{\Lambda}(\boldsymbol{x})\boldsymbol{W}^T(\boldsymbol{x})\boldsymbol{C}B(\boldsymbol{x})\widehat{\hat{\boldsymbol{u}}} - \boldsymbol{\Lambda}(\boldsymbol{x})\boldsymbol{\alpha}\bar{w}(\boldsymbol{x})\boldsymbol{\varphi}(\boldsymbol{x})\widehat{\hat{\boldsymbol{p}}})d\Omega \\
&+ \int_{\Omega^s} \rho\lambda_1(\boldsymbol{x})\lambda_2(\boldsymbol{x})\lambda_3(\boldsymbol{x})\boldsymbol{w}(\boldsymbol{x})(\hat{\boldsymbol{b}}(\boldsymbol{x}) - (i\omega)^2\boldsymbol{\Phi}(\boldsymbol{x})\widehat{\hat{\boldsymbol{u}}})d\Omega = 0
\end{aligned} \tag{39}$$

$$\begin{aligned}
&\int_{\Gamma^s} w_p(\boldsymbol{x})\boldsymbol{n}^T(\rho^f(i\omega)^2\boldsymbol{k} - \eta(i\omega)\boldsymbol{\alpha})\boldsymbol{\Lambda}(\boldsymbol{x})\boldsymbol{\Phi}(\boldsymbol{x})\widehat{\hat{\boldsymbol{u}}}d\Gamma \\
&+ \int_{\Gamma^s} w_p(\boldsymbol{x})\boldsymbol{n}^T\boldsymbol{k}(\boldsymbol{\Theta}(\boldsymbol{x})\bar{\boldsymbol{D}}(\boldsymbol{x})\widehat{\hat{\boldsymbol{p}}} - \rho^f\boldsymbol{\Lambda}(\boldsymbol{x})\hat{\boldsymbol{b}}(\boldsymbol{x}))d\Gamma \\
&- \int_{\Omega^s} \bar{\boldsymbol{w}}_p^T(\boldsymbol{x})\boldsymbol{\Lambda}(\boldsymbol{x})(\rho^f(i\omega)^2\boldsymbol{k} - \eta(i\omega)\boldsymbol{\alpha})\boldsymbol{\Phi}(\boldsymbol{x})\widehat{\hat{\boldsymbol{u}}}d\Omega \\
&- \int_{\Omega^s} \bar{\boldsymbol{w}}_p^T(\boldsymbol{x})(\boldsymbol{\Theta}(\boldsymbol{x})\boldsymbol{k}\bar{D}(\boldsymbol{x})\widehat{\hat{\boldsymbol{p}}} - \rho^f\boldsymbol{\Lambda}(\boldsymbol{x})\boldsymbol{k}\hat{b}(\boldsymbol{x}))d\Omega \\
&- \int_{\Omega^s} \frac{i\omega\eta}{M} w_p(\boldsymbol{x})\lambda_1(\boldsymbol{x})\lambda_2(\boldsymbol{x})\lambda_3(\boldsymbol{x})\boldsymbol{\varphi}(\boldsymbol{x})\widehat{\hat{\boldsymbol{p}}}d\Omega = 0
\end{aligned} \tag{40}$$

Thus, the sets of Equations (39) and (40) are the required equations at each subdomain for obtaining the unknown functions, which are three displacement components and pressure.

In this analysis, the local subdomain Ω^s centered at node I is considered a sphere with radius $r^s = \delta^s d^I$, where δ^s is a dimensionless size for the spherical subdomain, and d^I is the characteristic length that is the average nodal spacing between neighboring nodes in the vicinity of node I and node I. The support domain Ω^Q used for construction of P-RPIM shape functions is also a sphere with radius r^Q, which is given by $r^Q = \delta^Q d^I$, where δ^Q is a dimensionless size of the spherical support domain.

The discretized weak forms (39) and (40) for the saturated porous medium via Biot's formulation can be rewritten in the form of stiffness matrix, unknown, and force vectors as follows:

$$\begin{bmatrix} \boldsymbol{K}_j^{11} & \boldsymbol{K}_j^{12} \\ \boldsymbol{K}_j^{21} & \boldsymbol{K}_j^{22} \end{bmatrix} \begin{Bmatrix} \widehat{\hat{\boldsymbol{u}}} \\ \widehat{\hat{\boldsymbol{p}}} \end{Bmatrix} = \begin{Bmatrix} \boldsymbol{F}_j^1 \\ \boldsymbol{F}_j^2 \end{Bmatrix} \tag{41}$$

where

$$\begin{aligned}
\boldsymbol{K}_j^{11} &= \int_{\Gamma^s} \boldsymbol{w}(\boldsymbol{x})\bar{\boldsymbol{N}}(\boldsymbol{x})\boldsymbol{C}\bar{B}(\boldsymbol{x})d\Gamma - \int_{\Gamma^s} \boldsymbol{w}(\boldsymbol{x})\bar{\boldsymbol{N}}(\boldsymbol{x})\bar{\boldsymbol{\alpha}}\varphi(\boldsymbol{x})d\Gamma \\
&\quad - \int_{\Omega^s} (\boldsymbol{\Lambda}(\boldsymbol{x})\boldsymbol{W}^T(\boldsymbol{x})\boldsymbol{C}B(\boldsymbol{x}))d\Omega - \int_{\Omega^s} \rho(i\omega)^2\lambda_1(\boldsymbol{x})\lambda_2(\boldsymbol{x})\lambda_3(\boldsymbol{x})\boldsymbol{w}(\boldsymbol{x})\boldsymbol{\Phi}(\boldsymbol{x})d\Omega \\
\boldsymbol{K}_j^{12} &= -\int_{\Gamma^s} \boldsymbol{w}(\boldsymbol{x})\bar{\boldsymbol{N}}(\boldsymbol{x})\bar{\boldsymbol{\alpha}}\varphi(\boldsymbol{x})d\Gamma + \int_{\Omega^s} \boldsymbol{\Lambda}(\boldsymbol{x})\boldsymbol{\alpha}\bar{w}(\boldsymbol{x})\boldsymbol{\varphi}(\boldsymbol{x})d\Omega \\
\boldsymbol{K}_j^{21} &= \int_{\Gamma^s} w_p(\boldsymbol{x})\boldsymbol{n}^T(\rho^f(i\omega)^2\boldsymbol{k} - \eta(i\omega)\boldsymbol{\alpha})\boldsymbol{\Lambda}(\boldsymbol{x})\boldsymbol{\Phi}(\boldsymbol{x})d\Gamma \\
&\quad - \int_{\Omega^s} \bar{\boldsymbol{w}}_p^T(\boldsymbol{x})\boldsymbol{\Lambda}(\boldsymbol{x})(\rho^f(i\omega)^2\boldsymbol{k} - \eta(i\omega)\boldsymbol{\alpha})\boldsymbol{\Phi}(\boldsymbol{x})d\Omega
\end{aligned}$$

$$
\begin{aligned}
\boldsymbol{K}_j^{22} &= \int_{\Gamma^s} w_p(\boldsymbol{x})\boldsymbol{n}^T\boldsymbol{k}\Theta(\boldsymbol{x})\bar{\boldsymbol{D}}(\boldsymbol{x})d\Gamma - \int_{\Omega^s} \bar{\boldsymbol{w}}_p^T(\boldsymbol{x})\boldsymbol{\Theta}(\boldsymbol{x})\boldsymbol{k}\bar{D}(\boldsymbol{x})d\Omega \\
&\quad - \int_{\Omega^s} \frac{i\omega\eta}{M} w_p(\boldsymbol{x})\lambda_1(\boldsymbol{x})\lambda_2(\boldsymbol{x})\lambda_3(\boldsymbol{x})\boldsymbol{\varphi}(\boldsymbol{x})d\Omega \\
\boldsymbol{F}_j^1 &= -\int_{\Gamma^s-\Gamma_i^s} \boldsymbol{w}(\boldsymbol{x})\bar{\boldsymbol{N}}(\boldsymbol{x})\boldsymbol{C}\bar{B}(\boldsymbol{x})\widehat{\boldsymbol{u}}d\Gamma + \int_{\Gamma^s-\Gamma_i^s} \boldsymbol{w}(\boldsymbol{x})\bar{\boldsymbol{N}}(\boldsymbol{x})\bar{\boldsymbol{\alpha}}\varphi(\boldsymbol{x})\widehat{\boldsymbol{p}}d\Gamma \\
&\quad - \int_{\Omega^s} \rho\lambda_1(\boldsymbol{x})\lambda_2(\boldsymbol{x})\lambda_3(\boldsymbol{x})\boldsymbol{w}(\boldsymbol{x})\hat{\boldsymbol{b}}(\boldsymbol{x})d\Omega \\
\boldsymbol{F}_j^2 &= -\int_{\Gamma^s-\Gamma_i^s} w_p(\boldsymbol{x})\boldsymbol{n}^T(\rho^f(i\omega)^2\boldsymbol{k} - \eta(i\omega)\boldsymbol{\alpha})\boldsymbol{\Lambda}(\boldsymbol{x})\boldsymbol{\Phi}(\boldsymbol{x})\widehat{\boldsymbol{u}}d\Gamma \\
&\quad - \int_{\Gamma^s-\Gamma_i^s} w_p(\boldsymbol{x})\boldsymbol{n}^T\boldsymbol{k}(\boldsymbol{\Theta}(\boldsymbol{x})\bar{\boldsymbol{D}}(\boldsymbol{x})\widehat{\boldsymbol{p}} - \rho^f\boldsymbol{\Lambda}(\boldsymbol{x})\hat{\boldsymbol{b}}(\boldsymbol{x}))d\Gamma - \int_{\Omega^s} \bar{\boldsymbol{w}}_p^T(\boldsymbol{x})\rho^f\boldsymbol{\Lambda}(\boldsymbol{x})\boldsymbol{k}\hat{b}(\boldsymbol{x})d\Omega
\end{aligned} \tag{42}
$$

To numerically calculate the stiffness and force components, it would be appropriate to use the numerical integration methods proposed in refs. 64, 65, in which the uniform distributions of computational points over the spherical shell and planar annulus are introduced.

If the material is considered to be pure elastic instead of poroelastic, then the media cannot support fluid flow inside the solid. In this case, the governing equations for flow of fluid are independent from the deformation of the solid skeleton. In this case, the Equations (39) and (40) will be separated, and (39) becomes the governing equation of the elastodynamic problem. To this end, it suffices to put $\boldsymbol{\alpha} = 0$ in Equation (39). So, the discretized weak forms for transversely isotropic elastic problems can be written as:

$$
\begin{aligned}
&\textstyle\int_{\Gamma^s} \boldsymbol{w}(\boldsymbol{x})\bar{\boldsymbol{N}}(\boldsymbol{x})\boldsymbol{C}\bar{B}(\boldsymbol{x})\widehat{\boldsymbol{u}}d\Gamma - \int_{\Omega^s} \boldsymbol{\Lambda}(\boldsymbol{x})\boldsymbol{W}^T(\boldsymbol{x})\boldsymbol{C}B(\boldsymbol{x})\widehat{\boldsymbol{u}}d\Omega \\
&+ \textstyle\int_{\Omega^s} \rho\lambda_1(\boldsymbol{x})\lambda_2(\boldsymbol{x})\lambda_3(\boldsymbol{x})\boldsymbol{w}(\boldsymbol{x})(\hat{\boldsymbol{b}}(\boldsymbol{x}) - (i\omega)^2\boldsymbol{\Phi}(\boldsymbol{x})\widehat{\boldsymbol{u}})d\Omega = 0
\end{aligned} \tag{43}
$$

In this case, there are three degrees of freedom for each nodal point.

4.3 | The norm of error and problem-solving scheme

To improve the accuracy of the analysis in the near field, one can increase the density of nodes within any region with high variation of stress/displacement such as the regions embraced the loading area or the regions containing stress singularity. The process of improving the numerical analysis can be done by an error analysis. First, by the error analysis the regions with higher errors are distinguished and then the accuracy is improved with the use of refinement methods. The refinement may be done by adding new nodes or using high order of interpolation (the higher order of polynomial basis in P-RPIM) corresponding to the norm of error. The error analysis can be done by the approach proposed by Chung and Belytschko[56] where L_2-norm of error is used to evaluate the error in the form of energy norm at each subdomain as

$$
\|e^s\| = \left[\frac{1}{2}\int_{\Omega^s} (\boldsymbol{\sigma}^e(\boldsymbol{x}))^T C^{-1}\boldsymbol{\sigma}^e(\boldsymbol{x})d\Omega\right]^{1/2} \tag{44}
$$

where $\boldsymbol{\sigma}^e(\boldsymbol{x}) = \boldsymbol{\sigma}^p(\boldsymbol{x}) - \boldsymbol{\sigma}^h(\boldsymbol{x})$ and $\boldsymbol{\sigma}^p$ is the stresses obtained either with the stresses obtained from the previous analysis in the repetitive procedure, or the analytical stresses (if exists), and $\boldsymbol{\sigma}^h(\boldsymbol{x})$ is the approximated stress tensor. The energy norm for the whole domain is obtained in the form of the sum of the square of all subdomains' energy norms. The relative error can be calculated as

$$
R^e = \frac{\|e\|}{\|E\|} \tag{45}
$$

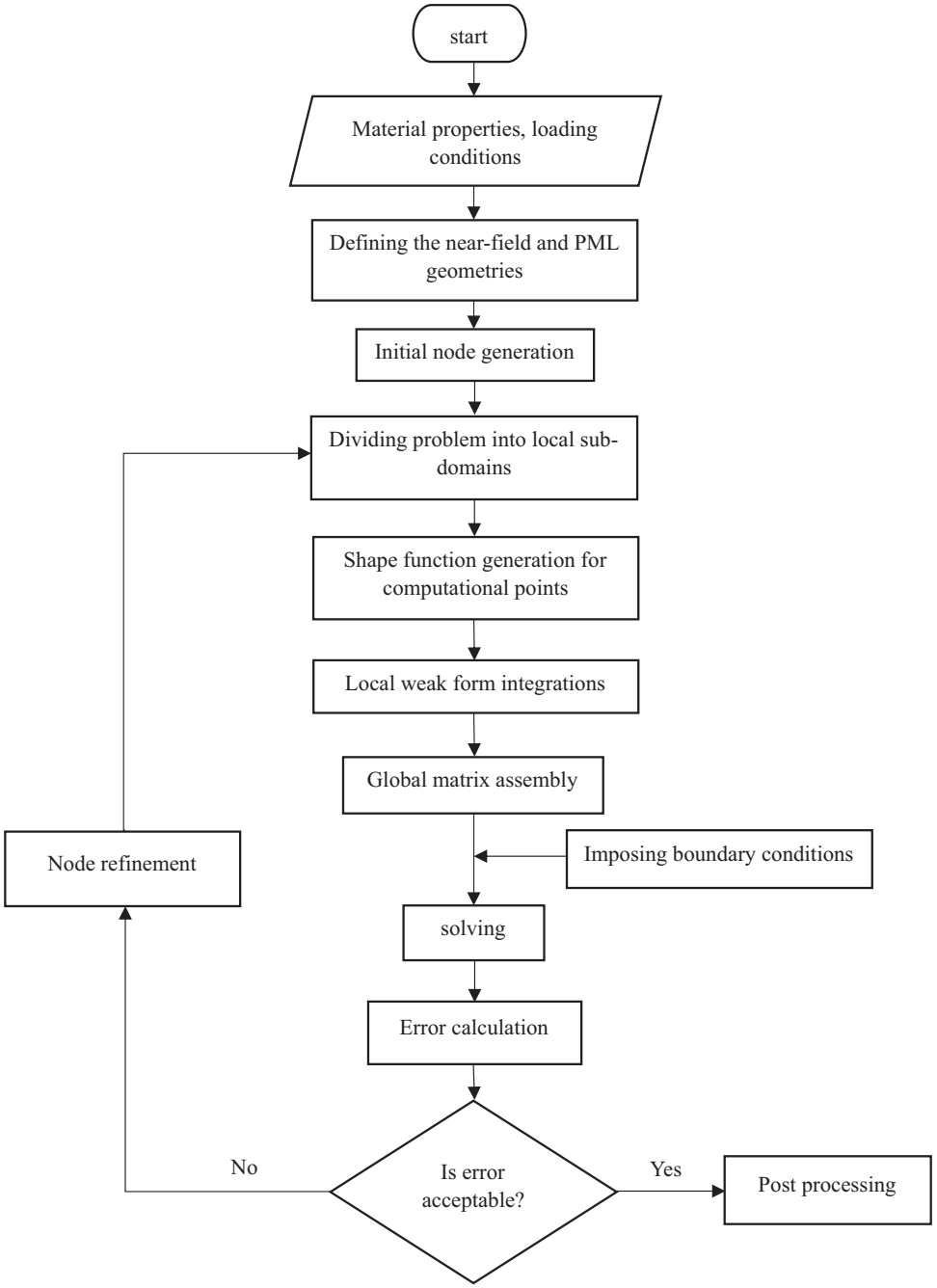

FLOW CHART 1 The steps to perform the PML based MLPG method. MLPG, meshless local Petrov–Galerkin; PML, perfectly matched layer.

where $\|E\|$ is calculated by substituting $\boldsymbol{\sigma}^p(\boldsymbol{x})$ for $\boldsymbol{\sigma}^e(\boldsymbol{x})$ in (44). At the end of each analysis the relative error is controlled, and the geometry is refined until $R^e < \varepsilon$ in which ε is a desired control value. The refinement would be started in the area where its local energy norm is dominant.

In summary, according to Flow chart 1, the steps to perform the MLPG method for various problems are as follows:

1. Defining the data required for the problem
   - Defining the domain geometry such as the near field and the PML
   - Defining the material properties
   - Defining the BCs
   - Defining the transfer functions and parameters of them

- Considering N nodes inside the domain Ω and on its boundary Γ
- Determining the shape and size of the support domain Ω^Q in such a way that at least a certain number of nodal points are located in it
- Dividing the domain Ω into some local subdomains Ω^s
- Defining the computational points and their corresponding weights
- Defining the radial and polynomial basis functions and choosing the method of generating shape functions

2. Assembling the stiffness matrix and solving the system of equations
   - Loop over the nodes to form a stiffness matrix for each node
   - Defining a local subdomain for each node
   - Creating a loop for computing the integrals involved in the weak form over the Gaussian points
   - Defining the support domain for each Gaussian point and calculating shape functions
   - Assembling the system of stiffness equations for all Gaussian points
   - Solving the resulting system of equations
3. Obtaining the output and postprocessing the results

In the next section, based on the presented formulation and procedure some examples are solved.

5 | NUMERICAL RESULTS

To model the domain of interest for performing numerical analysis, the near field, PML, transfer functions, and its appropriate BCs should be defined. The near field (Ω_N) and PML (Ω_P) are respectively considered as a cube and a finite band around it as follows,

$$\begin{aligned}\Omega_N &= \{(x_1, x_2, x_3) |\, |x_1| < x_N, |x_2| < x_N, 0 < x_3 < x_N\}\\ \Omega_P &= \Omega - \Omega_N\\ \Omega &= \{(x_1, x_2, x_3) |\, |x_1| < x_N + x_P, |x_2| < x_N + x_P, 0 < x_3 < x_N + x_P\}\end{aligned} \tag{46}$$

where Ω is the total domain for the interested BVP and Γ denotes its corresponding boundary. In addition, x_N and x_P are the sizes of the near field and the PML, respectively.

In order not to face inappropriate conditions in the process of numerical calculations such as ill conditioning, the transfer function (3) should be defined in such a way that the responses to be attenuated smoothly along the PML. To this end, a simple polynomial form is used to define the transfer functions. These functions are as follows:

$$\begin{aligned}\lambda_i(x_i) &= \alpha_i(x_i) + \frac{1}{i\omega}\beta_i(x_i), \qquad i = 1, 2, 3\\ \alpha_i(x_i) &= 1 + f^{\alpha}_{x_i}\frac{(x_i - x_N)^m}{x_P^m}\\ \beta_i(x_i) &= f^{\beta}_{x_i}\frac{(x_i - x_N)^m}{x_P^m}\end{aligned} \tag{47}$$

in which $f^{\alpha}_{x_i}$ and $f^{\beta}_{x_i}$ are positive real constants, and m is a non-negative integer. The functions (47) satisfy all necessary conditions for the transferring function discussed in Section 3.1. Note that the attenuation power is directly proportional to $f^{\alpha}_{x_i}$ and $f^{\beta}_{x_i}$; however, inversely to m. Also, the PML depth, where the energy is attenuated through, would affect the response functions in the near field. As the depth increases, the amplitude of forward wave decreases, and so, it reflects with smaller amplitude from the far boundary of PML. But the large PML increases the cost of numerical analysis.

Furthermore, the radial base function used here is as follows:

$$R_k(\boldsymbol{x}, \boldsymbol{\xi}) = \sqrt{c_0^2 + c_1^2(x_1 - x_{1;k})^2 + c_2^2(x_2 - x_{2;k})^2 + c_3^2(x_3 - x_{3;k})^2} \tag{48}$$

TABLE 1 Material coefficients of saturated porous transversely isotropic half space.[66]

C_{1111} (N/mm^2)	C_{3333} (N/mm^2)	C_{1313} (N/mm^2)	C_{1212} (N/mm^2)	C_{1133} (N/mm^2)	n %	K_s (N/mm^2)	K_f (N/mm^2)	ρ_s (kg/m^3)	ρ_f (kg/m^3)	k_1 (m^2)	k_3 (m^2)	η (Pa S)
9570	8320	3000	4190	2330	20	35,000	2250	2600	1000	10^{-12}	10^{-13}	10^{-3}

in which c_0 is a dimensionless shape parameter, and c_i s are scale factors. According to Equations (48) and (31) R_k is a symmetric matrix.

The number of local subdomains should be large enough in such a way that the unknowns of the problem are determined uniquely. It is clear that the error of the approximations depends on the number of the local subdomain Ω^s, their sizes, and the gap/overlap of adjacent subdomains. Too large or too small size of subdomains would result in less accuracy. Also, the overlap of subdomains can improve the accuracy of results (see[63] for more details). On the other hand, the whole number of nodes and subdomains for analysis may depend on the problem geometry and BCs. The process of numerical analysis is an iterative procedure based on error analysis. After performing the analysis at the first stage with a uniform nodal distribution and a selected set of MLPG support domains, and then advancing further by a second analysis with a nodal refinement and new set of MLPG support domains, the total relative error of the second stage with respect to the first one is determined, and is compared with an acceptable error, say the reference error. If the computed error is larger than the reference error, then the refinement procedure should be repeated further until an acceptable error is reached for the final refined nodal distribution its associated selection of support domains.

A suitable vector space for weight functions should be selected for numerical evaluations of the integrals involved in weak forms. In the case which the size of the local subdomains Ω^s is small, the constant weight function would be appropriate, and the accuracy would not be significantly affected by that. Thus, the weight functions are considered as:

$$w_i = w_p = \begin{cases} 1, \boldsymbol{x} \in \Omega^s \cup \Gamma^s \\ 0, \quad \boldsymbol{x} \notin \Omega^s \end{cases} \quad i = 1, 2, 3 \tag{49}$$

The advantage of these weight functions is that their derivatives are zero, which leads to simple local weak forms.

To verify the numerical calculations, some of the numerical results obtained from the presented meshless method are compared with the analytical solutions reported in some papers. The error analysis is done for a half-space subjected to a uniform horizontal patch load and the resulted geometry is used for other problems. It should be noted that the dimensionless circular frequency $\omega_0 = \omega a \sqrt{\rho / C_{1313}}$ is used for numerical calculations.

In the following, in the absence of body forces, several problems are examined. For this purpose, a homogeneous saturated porous transversely isotropic half-space filled by the material given in Table 1 is considered. The material properties are borrowed from.[66]

5.1 | Stress wave propagation

Consider a saturated porous half-space with transversely isotropic properties as given in Table 1. This half-space is vibrated by a surface force tremor f and pure fluid pressure p on Γ_f,

$$\boldsymbol{f}(\boldsymbol{x}, t) = \hat{\boldsymbol{f}}(\boldsymbol{x}) e^{i\omega t}, p(\boldsymbol{x}, t) = \hat{p}(\boldsymbol{x}) e^{i\omega t}, \ \boldsymbol{x} \in \Gamma_f \tag{50}$$

According to the described procedure in Flow chart 1, the half-space is divided into two separated regions, a near field and a far-field, and the far-field is replaced with a PML. As the responses in the PML are not desired, one may consider either Dirichlet or Neumann BC for both skeleton and fluid at the end of the PML. Here, Dirichlet BCs $\boldsymbol{u} = 0$ and $p = 0$ are considered at the end of the PML. Consequently, the BCs of the problem in the frequency domain are summarized as follows:

$$\boldsymbol{t}^{\circ}(\boldsymbol{x}) = \hat{\boldsymbol{f}}(\boldsymbol{x}) \, , p^{\circ}(\boldsymbol{x}) = \hat{p}(\boldsymbol{x}) \, , \ \boldsymbol{x} \in \Gamma_f$$

$$\boldsymbol{u}^{\circ}(\boldsymbol{x}) = \boldsymbol{0} \, , p^{\circ}(\boldsymbol{x}) = 0, \ \boldsymbol{x} \in \Gamma_{PML} \tag{51}$$

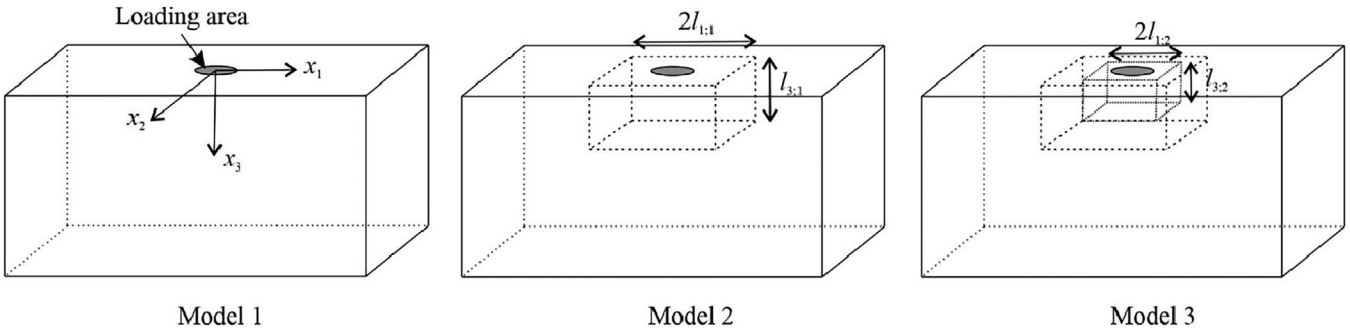

FIGURE 5 Refinement of nodes around the loading area for improving the meshless analysis results. Model1: uniform node distribution, Model 2: adding some nodes to Model 1 in the specific region, and Model 3: adding some further nodes to Model 2 in the specific region.

where Γ_{PML} is the boundary of the domain at the end of the PML,

$$\Gamma_{PML} = \{(x_1, x_2, x_3) | x_1 = \pm(x_N + x_P), x_2 = \pm(x_N + x_P), x_3 = (x_N + x_P)\} \tag{52}$$

It should be noted that the amplitude of the progressive wave is sufficiently attenuated in the PML. Thus, there will be no reflected wave from its far boundary, and the BCs (51) do not affect the accuracy of the responses in the near field. The BCs of the problem include two parts Γ_{up} and Γ_{tp}. As a result, the boundary of each local subdomain, depending on position of the local subdomain in the global domain, consists of three parts, $\Gamma^s = \Gamma_i^s \cup \Gamma_{up}^s \cup \Gamma_{tp}^s$.

In the previous section, the discretized weak forms for the saturated porous medium were obtained using Biot's formulation. Considering the weight function according to (49), the Equations (41) for j-th local subdomain are:

$$\begin{bmatrix} \boldsymbol{K}_j^{11} & \boldsymbol{K}_j^{12} \\ \boldsymbol{K}_j^{21} & \boldsymbol{K}_j^{22} \end{bmatrix} \begin{Bmatrix} \widehat{\hat{\boldsymbol{u}}} \\ \widehat{\hat{\boldsymbol{p}}} \end{Bmatrix} = \begin{Bmatrix} \boldsymbol{F}_j^1 \\ \boldsymbol{F}_j^2 \end{Bmatrix} \tag{53}$$

where

$$\begin{aligned}
\boldsymbol{K}_j^{11} &= \int_{\Gamma^s} \boldsymbol{w}(\boldsymbol{x}) \bar{\boldsymbol{N}}(\boldsymbol{x}) \boldsymbol{C} \bar{\boldsymbol{B}}(\boldsymbol{x}) d\Gamma - \int_{\Omega^s} \rho (i\omega)^2 \lambda_1(\boldsymbol{x}) \lambda_2(\boldsymbol{x}) \lambda_3(\boldsymbol{x}) \boldsymbol{w}(\boldsymbol{x}) \boldsymbol{\Phi}(\boldsymbol{x}) d\Omega \\
\boldsymbol{K}_j^{12} &= -\int_{\Gamma^s} \boldsymbol{w}(\boldsymbol{x}) \bar{\boldsymbol{N}}(\boldsymbol{x}) \boldsymbol{\Lambda}(\boldsymbol{x}) \bar{\boldsymbol{\alpha}} \varphi(\boldsymbol{x}) d\Gamma \\
\boldsymbol{K}_j^{21} &= \int_{\Gamma^s} w_p(\boldsymbol{x}) \boldsymbol{n}^T (\rho^f (i\omega)^2 \boldsymbol{k} - \eta (i\omega) \boldsymbol{\alpha}) \boldsymbol{\Lambda}(\boldsymbol{x}) \boldsymbol{\Phi}(\boldsymbol{x}) d\Gamma \\
\boldsymbol{K}_j^{22} &= \int_{\Gamma^s} w_p(\boldsymbol{x}) \boldsymbol{n}^T \boldsymbol{k} \Theta(\boldsymbol{x}) \bar{\boldsymbol{D}}(\boldsymbol{x}) d\Gamma - \int_{\Gamma^s} \frac{i\omega\eta}{M} w_p(\boldsymbol{x}) \lambda_1(\boldsymbol{x}) \lambda_2(\boldsymbol{x}) \lambda_3(\boldsymbol{x}) \boldsymbol{\varphi}(\boldsymbol{x}) d\Gamma \\
\boldsymbol{F}_j^1 &= -\int_{\Gamma^s - \Gamma_i^s} \boldsymbol{w}(\boldsymbol{x}) \bar{\boldsymbol{N}}(\boldsymbol{x}) \boldsymbol{C} \bar{\boldsymbol{B}}(\boldsymbol{x}) \widehat{\hat{\boldsymbol{u}}} d\Gamma = -\int_{\Gamma_i^s} \boldsymbol{t}^\circ d\Gamma \\
\boldsymbol{F}_j^2 &= 0
\end{aligned} \tag{54}$$

In the following, the numerical results for some special loading cases are presented. Consider the loading area in the form of a circular patch of radius a_0. If $\hat{\boldsymbol{f}} = P_0 \boldsymbol{e}_3$ (P_0 is constant), this problem is an axially symmetric and torsion free problem due to symmetry of loading and material properties with respect to the x_3-axis, while for $\hat{\boldsymbol{f}} = R_0 \boldsymbol{e}_1$ the problem is asymmetric. The size of near field and the PML depth are selected as $x_N = x_P = 10a_0$. Reducing the semi-infinite far-field to a finite depth layer ($x_P = 10a_0$) is of great interest.

As the analytical solution for the half-space subjected to a uniform patch load is in hand,[10] it is compared with the corresponding numerical solution in the case of the horizontal patch load. First, the numerical analysis is done with a uniform node distribution, and the related error is estimated. As expected, the relative error is about 20 percent, which is not accepted, and to improve the accuracy of the numerical results, a more node density is needed in the region near the loading area due to high stress gradient in this region. The refining procedure is done until a desired

TABLE 2 Relative errors resulted from the different models for the uniform horizontal patch load case.

Model	Number of nodes	The relative error
1. Uniform node distribution ($d^I = 2$)	4851	20%
2. Refinement of Model 1 ($l_{i,1} = 5, d^I_{i,1} = 1, i = 1, 2, 3$)	5577	5%
3. Refinement of Model 2 ($l_{i,2} = 2, d^I_{i,2} = 0.5, i = 1, 2, 3$)	5982	1.2%

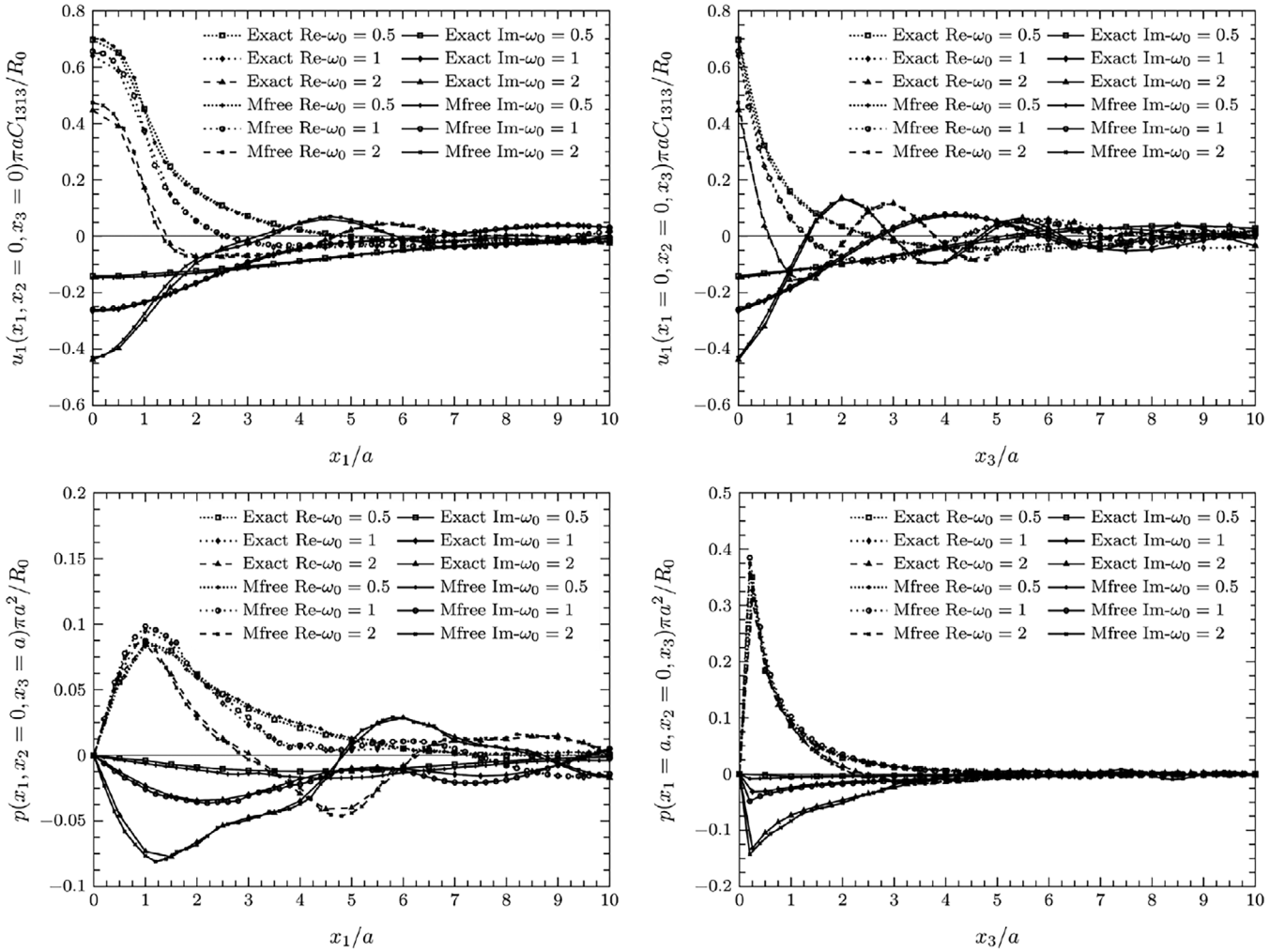

FIGURE 6 The transversely isotropic poroelastic half-space subjected to circular uniform horizontal force.

numerical result achieved (see Figure 5). The corresponding relative errors for two steps are presented in Table 2. It is seen that the relative error in the third model (the second refinement) with 5882 nodes is 1.2%, which is acceptable. Thus, the other analysis is proceeded with the node distribution obtained from refinement of Model 2. It should be noted that just the subdomain located in the near field is participated in the error analysis and the analysis in each step is done independently. In addition, the analytical stresses are used to calculate the energy norm of error in Equation (44).

The numerical results for three special cases defined as (i) vertical uniform patch load ($\hat{\boldsymbol{f}} = P_0\boldsymbol{e}_3$), (ii) horizontal uniform patch load ($\hat{\boldsymbol{f}} = R_0\boldsymbol{e}_1$), and (iii) linear patch load ($\hat{\boldsymbol{f}} = Q_0 x_1 \boldsymbol{e}_1$) are depicted in Figures 6–8. Considering the values of $f^{\alpha}_{x_i} = 1$, $f^{\beta}_{x_i} = 1.5$, and $m = 2$ for the parameters of the stretching function (47), $\delta^s = 0.55$ (which represents 5% overlap for the adjacent subdomains), and $\delta^Q = 2$, the graphs are presented. Also, the iso-stress curves are shown in Figure 9.

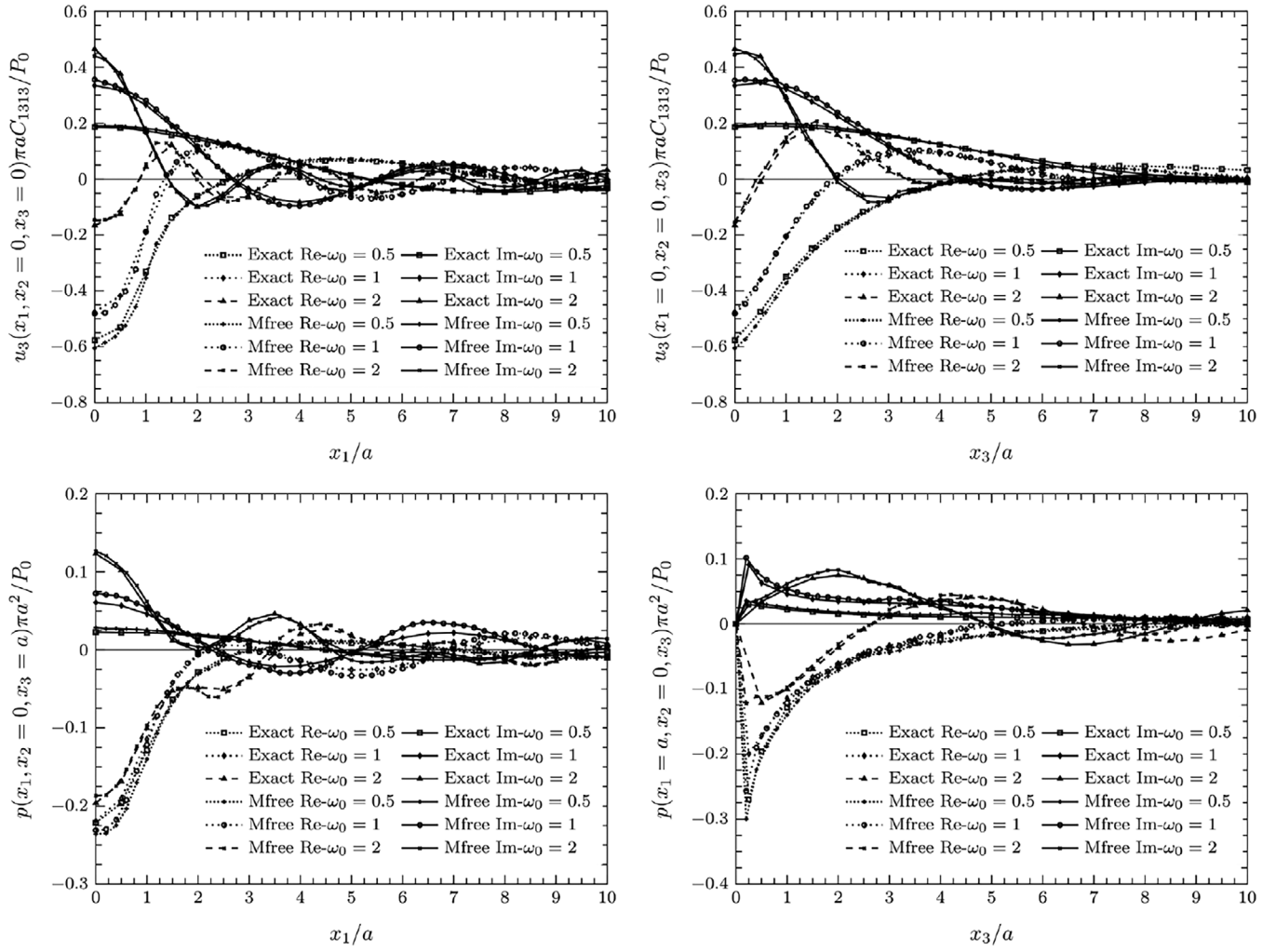

FIGURE 7 The transversely isotropic poroelastic half-space subjected to circular uniform vertical force.

5.2 | Forced vibration of a rigid foundation

If the poroelastic half-space is excited by a permeable rigid foundation, the BCs are as:

$$\begin{aligned} u_1(\boldsymbol{x}) &= (\Delta_1 - x_2\psi_3)e^{i\omega t} \\ u_2(\boldsymbol{x}) &= (\Delta_2 - x_1\psi_3)e^{i\omega t} \\ u_3(\boldsymbol{x}) &= (\Delta_3 - x_1\psi_2 + x_2\psi_1)e^{i\omega t}, \qquad \boldsymbol{x} \in \Gamma_\Delta \\ p(\boldsymbol{x}) &= \hat{p}(\boldsymbol{x})e^{i\omega t} \end{aligned} \tag{55}$$

and

$$\begin{aligned} &\sigma_{x_i x_3}(\boldsymbol{x}) = 0, i = 1, 2, 3, \quad \boldsymbol{x} \in \Gamma_{tp} \\ &p(\boldsymbol{x}) = 0, \qquad\qquad\qquad\quad \boldsymbol{x} \in \Gamma_{tp} \end{aligned} \tag{56}$$

where Δ_i and ψ_i $(i = 1, 2, 3)$ are the displacements and rotations with respect to x_i-axis, Γ_Δ is the surface of the half-space that is in contact with the foundation, and Γ_{tp} is the rest part of the body surface. Also, the BCs for the end of the PML, as expressed in (51), are $\boldsymbol{u} = 0$ and $p = 0$. The numerical results for the special cases (i) forced horizontal vibration ($u_1 = \Delta_1$), (ii) forced vertical vibration ($u_3 = \Delta_3$), (iii) rocking vibration ($u_3 = -x_1\psi_2$), and (iv) torsion vibration ($u_1 = -x_2\psi_3$) of a fully permeable rigid disk are solved, and then, depicted in Figures 10–13. As mentioned in previous section, in case $\boldsymbol{u} = \Delta_3\boldsymbol{e}_3$, the problem is an axially symmetric and torsion-free problem.

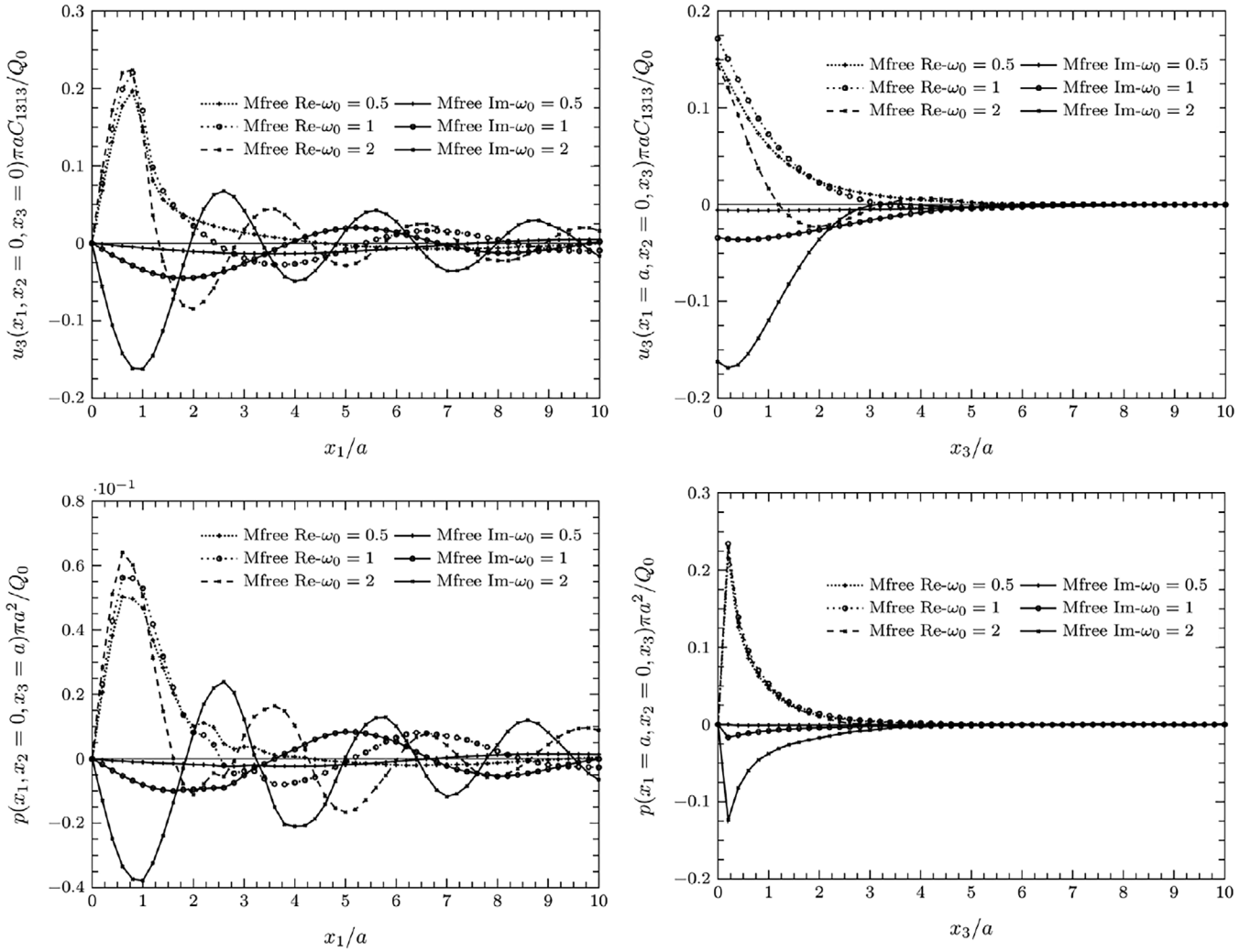

FIGURE 8 The transversely isotropic poroelastic half-space subjected to circular rocking force.

6 | CONCLUSIONS

In this paper, the wave propagation in the transversely isotropic poroelastic half-space in the framework of $\boldsymbol{u} - p$ formulation of Biot has been investigated numerically with the use of MLPG method and the following results have been obtained:

1. A truncated subset of the original domain, namely the near field, has been considered to prepare the half-space for domain-based numerical analysis of wave propagation and to impose the radiation condition, and the rest of the half-space denoted as the far-field has been replaced by a PML. So, the energy propagated toward the PML is completely attenuated through it in such a way that there is no reflection toward the near field.
2. In order for the PML to be introduced correctly, a new family of the stretched coordinate functions has been introduced, and then, the governing equations and its weak forms have been obtained in the stretched coordinate system.
3. The global domain is divided into some subdomains, and then, the system of equations has been established by the set of local weak forms on the subdomains in order to obtain the response functions in the nodal points distributed within the domain and its boundary. The shape functions for each computational point are constructed with the use of the P-RPIM to numerically calculate the local weak forms.
4. The presented numerical process has been used to extract the responses for arbitrary time-harmonic traction/displacement vibrations. To investigate the stresses in the half-space due to the applied tractions, the iso-stress (equi-stress) surfaces have been illustrated.

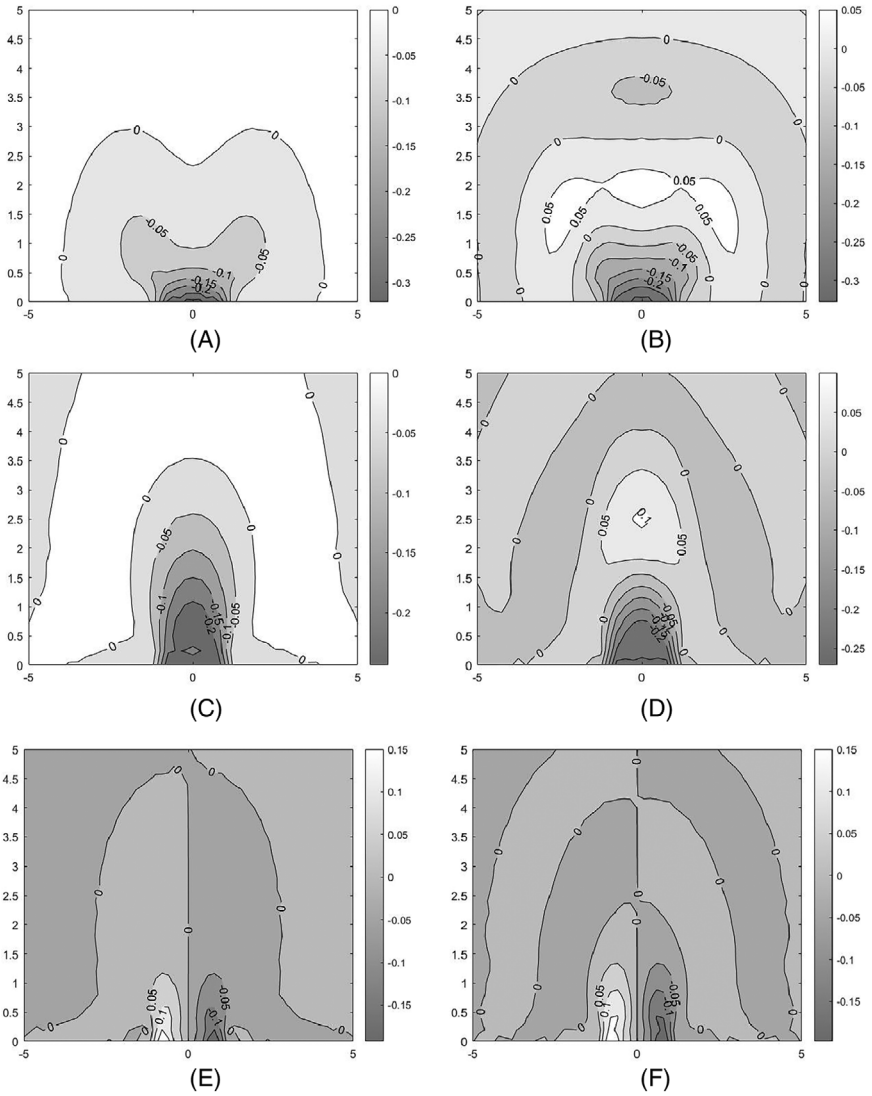

FIGURE 9 The iso-stress curves in x_1x_3-plane for the half-space subjected to the uniform horizontal patch load (A) $\sigma_{rz}, w_0 = 1$ and (B) $\sigma_{rz}, \omega_0 = 2$, the uniform vertical patch load (C) $\sigma_{zz}, w_0 = 1$ and (D) $\sigma_{zz}, \omega_0 = 2$, and the rocking patch load (E) $\sigma_{zz}, w_0 = 1$ and (F) $\sigma_{zz}, w_0 = 2$.

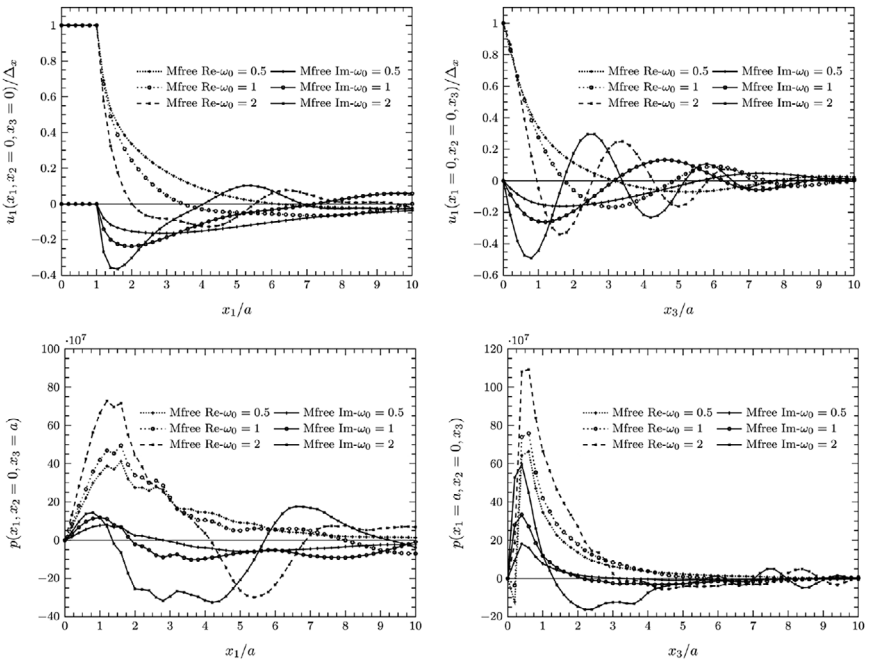

FIGURE 10 The transversely isotropic poroelastic half-space subjected to the horizontal disk vibration.

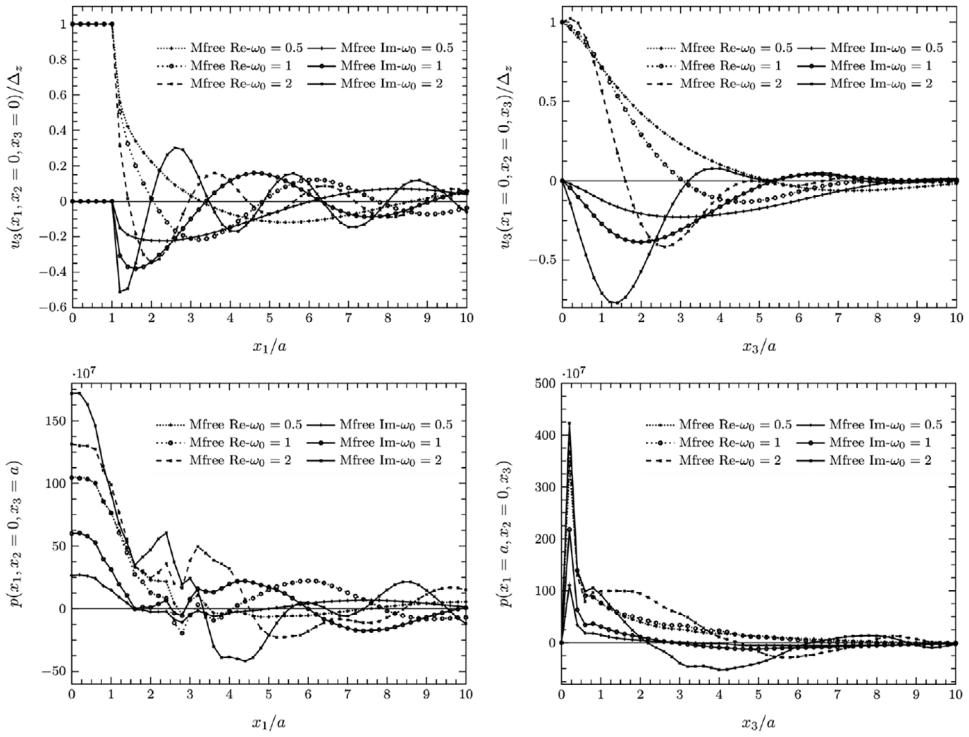

FIGURE 11 The transversely isotropic poroelastic half-space subjected to the vertical disk vibration.

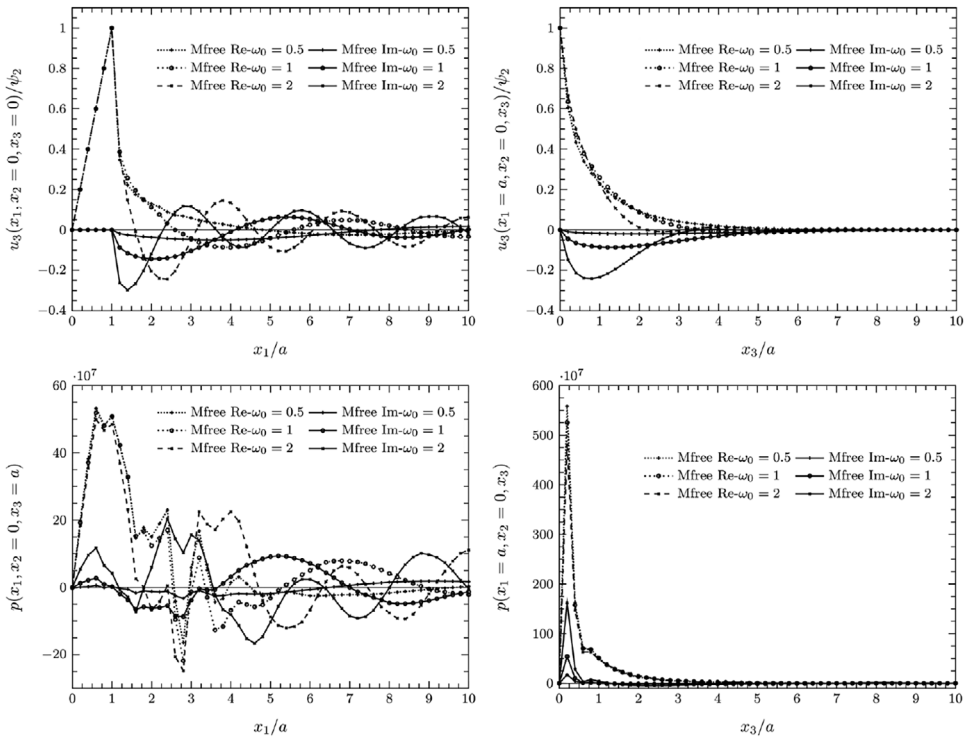

FIGURE 12 The transversely isotropic poroelastic half-space subjected to the rocking disk vibration.

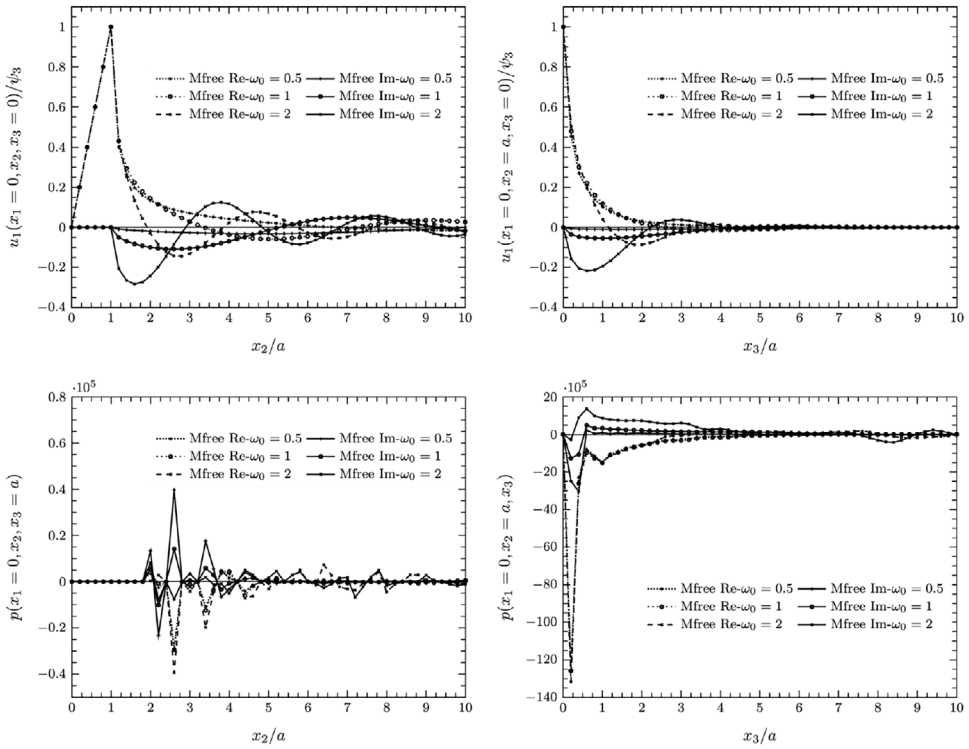

FIGURE 13 The transversely isotropic poroelastic half-space subjected to the torsion disk vibration.

5. By the proposed approach, a wide range of dynamic boundary-value problems with infinite/semi-infinite geometries filled with homogenous/layered isotropic/transversely isotropic materials can be solved in the time/frequency domains. Note that linear terms of strain tensor (Cauchy's strain tensor) are considered in the Biot's theory.

NOMENCLATURE

a_0	radius of circular loading
$\boldsymbol{b}$	body force
$\boldsymbol{C}$	elasticity tensor
e^s, E	errors
R^e	relative error
$\boldsymbol{f}$	force excitation
$\boldsymbol{F}$	force vector
$\boldsymbol{k}$	intrinsic permeability tensor
$\boldsymbol{K}$	stiffness function
l_s	size of refinement zone along s-axis
M	Biot's modulus
n	porosity
N	number of nodes
$\boldsymbol{n}, \boldsymbol{N}$	matrices consisting of normal vector components
p	pore fluid pressure
$\boldsymbol{P}$	polynomial basis functions
P_0, R_0	constant values
$\boldsymbol{q}$	fluid flow rate
$\boldsymbol{R}$	radial basis functions
t	time
$\boldsymbol{t}$	traction vector
$\boldsymbol{u}$	displacement vector of solid

w	relative displacement vector
$\boldsymbol{w}, w_p$	weight functions
$\boldsymbol{x}$	Cartesian coordinate system
$\tilde{\boldsymbol{x}}$	stretched coordinate system
$\boldsymbol{\alpha}$	Biot's effective stress tensor
α_s	scale function along s-axis
β_s	attenuation function
Γ	domain boundary
Γ^s	sub-domain boundary
$\boldsymbol{\Delta}$	forced displacement vector
ε	error control value
η	dynamic viscosity of the fluid
$\boldsymbol{\xi}$	nodal point
λ_s	stretching function along s-axis
$\boldsymbol{\Lambda}, \boldsymbol{\Theta}$	matrices consisting of stretching functions
ρ	mass density of the mixture
ρ^f	mass density of the fluid
ρ^s	mass density of the solid
$\boldsymbol{\sigma}$	total stress tensor of the solid skeleton
$\boldsymbol{\sigma}^s$	effective stress tensor
$\boldsymbol{\varphi}$	shape function vector
$\boldsymbol{\psi}$	forced rotation vector
ω	angular frequency
ω_0	dimensionless frequency
Ω	problem domain
Ω_N	near field
Ω_P	perfectly matched layer
Ω^Q	support domain
Ω^s	sub-domain
$.^h$	estimated value

ACKNOWLEDGMENTS

The partial support from the University of Tehran through 27840/1/09 to Morteza Eskandari-Ghadi during this work is gratefully acknowledged.

DATA AVAILABILITY STATEMENT

The data that support the findings of this study are available from the corresponding author upon reasonable request.

ORCID

Kamal Shaker https://orcid.org/0009-0007-0321-3940
Morteza Eskandari-Ghadi https://orcid.org/0000-0002-7008-0654

REFERENCES

1. Biot MA. Theory of elastic waves in a fluid-saturated porous solid. 1. Low frequency range. *J Acoust Soc Am*. 1956;28:168-178.
2. Biot MA. Mechanics of deformation and acoustic propagation in porous media. *J Appl Phys*. 1962;33:1482-1498. doi:10.1063/1.1728759
3. Zienkiewicz OC, Chang CT, Bettess P. Drained, undrained, consolidating and dynamic behaviour assumptions in soils. *Geotechnique*. 1980;30(4):385-395. doi:10.1680/geot.1980.30.4.385
4. Zienkiewicz OC, Shiomi T. Dynamic behaviour of saturated porous media; the generalized Biot formulation and its numerical solution. *Int J Numer Anal Methods Geomech*. 1984;8:71-96. doi:10.1002/nag.1610080106
5. Gorog S, Panneton R, Atalla N. Mixed displacement-pressure formulation for acoustic anisotropic open porous media. *J Appl Phys*. 1997;82:4192-4196. doi:10.1063/1.366221
6. Ding B, Cheng AH-D, Chen Z. Fundamental solutions of poroelastodynamics in frequency domain based on wave decomposition. *J Appl Mech*. 2013;80(6):061021. doi:10.1115/1.4023692

7. Kazi-Aoual MN, Bonnet G, Jouanna P. Green's functions in an infinite transversely isotropic saturated poroelastic medium. *J Acoust Soc Am*. 1988;84:1883-1889.
8. Taguchi I, Kurashige M. Fundamental solutions for a fluid-saturated, transversely isotropic, poroelastic solid. *Int J Numer Anal Methods Geomech*. 2002;26(3):299-321.
9. Kumar R, Garg NR, Miglani A. Dynamic behaviour of an anisotropic liquid-saturated porous medium in frequency domain. *J Sound Vib*. 2004;275(3–5):877-891.
10. Sahebkar K, Eskandari-Ghadi M. Time-harmonic response of saturated porous transversely isotropic half-space under surface tractions. *J Hydrol*. 2016;537:61-73. doi:10.1016/j.jhydrol.2016.02.050
11. Sahebkar K, Eskandari-Ghadi M. Dynamic behaviour of an infinite saturated transversely isotropic porous media under fluid-phase excitation. *Soil Dyn Earthquake Eng*. 2018;107:390-406.
12. Jafarzadeh A, Eskandari-Ghadi M. Surface load dynamic solution of saturated transversely isotropic multilayer half-space. *Int J Numer Anal Methods Geomech*. 2019;25:1655-1685. doi:10.1002/nag.2904
13. Wang F, Ding T, Han X, Lv L. Dynamic green's functions for an anisotropic poroelastic half-space. *Int J Numer Anal Methods Geomech*. 2020;44:904-920.
14. Teymouri H, Khojasteh A, Rahimian M, Pak RYS. Wave motion in multi-layered transversely isotropic porous media by the method of potential functions. *Math Mech Solids*. 2020;25:108128651988392.
15. Ba Z, Wu M, Liang J. 3D dynamic responses of a multi-layered transversely isotropic saturated half-space under concentrated forces and pore pressure. *Appl Math Modell*. 2020;80:859-878.
16. Zhang Z, Pan E. Time-harmonic response of transversely isotropic and layered poroelastic half-spaces under general buried loads. *Appl Math Modell*. 2020;80:426-453.
17. Ba Z, Liang J, Lee VW, Ji H. 3D dynamic response of a multi-layered transversely isotropic half-space subjected to a moving point load along a horizontal straight line with constant speed. *Int J Solids Struct*. 2016;100-101:427-445. doi:10.1016/j.ijsolstr.2016.09.016
18. Ba Z, Liang J. Fundamental solutions of a multi-layered transversely isotropic saturated half-space subjected to moving point forces and pore pressure. *Eng Anal Boundary Elem*. 2017;76:40-58. doi:10.1016/j.enganabound.2016.12.006
19. Ai ZY, Wang XM, Zhao YZ. 3D dynamic analysis of layered transversely isotropic saturated media subjected to circular moving loads. *Appl Math Modell*. 2021;95:783-805. doi:10.1016/j.apm.2021.02.019
20. Ai ZY, Gu GL. Dynamic behaviour of layered transversely isotropic poroelastic media subjected to rectangular harmonic loads. *Int J Numer Anal Methods Geomech*. 2022;46:1941-1955. doi:10.1002/nag.3375
21. Zhang YL, Ai ZY, Zhao YZ, Ji WT, Gao GY. Analytical layer element solution for layered porous media subjected to non-axisymmetric transient loadings. *Appl Math Modell*. 2023;122:761-779. doi:10.1016/j.apm.2023.06.010
22. Liang J, Wu M, Ba Z, Sang Q. A reflection-transmission matrix method for time-history response analysis of a layered TI saturated site under obliquely incident seismic waves. *Appl Math Modell*. 2021;97:206-225. doi:10.1016/j.apm.2021.03.052
23. Lysmer J, Kuhlemeyer RL. Finite dynamic model for infinite media. *J Eng Mech Div*. 1969;95:859-877.
24. Tsynkov SV. Numerical solution of problems on unbounded domains. A review. *Appl Numer Math*. 1998;27:465-532.
25. Givoli D. *Numerical Methods For Problems In Infinite Domains*. Elsevier; 2013.
26. Clayton R, Engquist B. Absorbing boundary conditions for acoustic and elastic wave equations. *Bull Seismol Soc Am*. 1977;67:1529-1540.
27. Givoli D, Keller JB. Non-reflecting boundary conditions for elastic waves. *Wave Motion*. 1990;12:261-279.
28. Givoli D, Vigdergauz S. Artificial boundary conditions for 2D problems in geophysics. *Comput Methods Appl Mech Eng*. 1993;110(1-2):87-101.
29. Higdon RL. Absorbing boundary conditions for elastic waves. *Geophysics*. 1991;56(2):168-323.
30. Manolis GD, Beskos DE. *Boundary Element Methods in Elastodynamics*. Routledge; 1988.
31. Meza-Fajardo KC, Papageorgiou AS. Study of the accuracy of the multiaxial perfectly matched layer for the elastic-wave equation. *Bull Seismol Soc Am*. 2012;102(6):2458-2467.
32. Berenger J. A perfectly matched layer for the absorption of electromagnetic waves. *J Comput Phys*. 1994;114(2):185-200.
33. Taflove A, Hagness SC, Piket-May M. Computational electromagnetics: the finite-difference time-domain method. *The Electrical Engineering Handbook*. Elsevier Inc; 2005:629-670. doi:10.1016/B978-012170960-0/50046-3
34. Chew WC, Weedon WH. A 3D perfectly matched medium from modified Maxwell's equations with stretched coordinates. *Microwave Opt Technol Lett*. 1994;7:599-604.
35. Chew WC, Liu QH. Perfectly matched layers for elastodynamics: a new absorbing boundary condition. *J Comput Acoust*. 1996;4:341-359.
36. Hastings FD, Schneider JB, Broschat SL. Application of the perfectly matched layer (PML) absorbing boundary condition to elastic wave propagation. *J Acoust Soc Am*. 1996;100:3061-3069.
37. Liu QH. Perfectly matched layers for elastic waves in cylindrical and spherical coordinates. *J Acoust Soc Am*. 1999;105(4):2075-2084.
38. Basu U, Chopra AK. Perfectly matched layers for time-harmonic elastodynamics of unbounded domains: theory and finite-element implementation. *Comput Methods Appl Mech Eng*. 2003;192(11-12):1337-1375.
39. Basu U, Chopra AK. Perfectly matched layers for transient elastodynamics of unbounded domains. *Int J Numer Methods Eng*. 2004;59(8):1039-1074. doi:10.1002/nme.896
40. Zeng YQ, Liu QH. A staggered-grid finite-difference method with perfectly matched layers for poroelastic wave equations. *J Acoust Soc Am*. 2001;109:2571-2580. doi:10.1121/1.1369783
41. Fathi A, Poursartip B, Kallivokas LF. Time-domain hybrid formulations for wave simulations in three-dimensional PML-truncated heterogeneous media. *Int J Numer Methods Eng*. 2015;101(3):165-198. doi:10.1002/nme.4780

42. Zhang W, Taciroglu E. A novel Rayleigh-type viscoelastic perfectly-matched-layer for wave propagation analysis: formulation, implementation and application. *Comput Meth Appl Mech Eng*. 2021;383:113913.
43. François S, Goh H, Kallivokas LF. Non-convolutional second-order complex-frequency-shifted perfectly matched layers for transient elastic wave propagation. *Comput Meth Appl Mech Eng*. 2021;377:113704.
44. Belytschko T, Lu YY, Gu L. Element-free Galerkin methods. *Int J Numer Methods Eng*. 1994;37:229-256.
45. Atluri SN, Zhu T. A new meshless local Petrov-Galerkin (MLPG) approach in computational mechanics. *Comput Mech*. 1998;22:117-127. doi:10.1007/s004660050346
46. Liu GR, Gu YT. A point interpolation method for two-dimensional solids. *Int J Numer Methods Eng*. 2001;50:937-951.
47. Perazzo F, Miquel J. *Interpolation in the FPM*. *Elsevier*.
48. Atluri SN. *The Meshless Method (MLPG) for Domain and BIE Discretizations*. Tech. Science Press; 2004.
49. Lucy LB. A numerical approach to the testing of the fission hypothesis. *Astron J*. 1977;82:1013-1024.
50. Gingold RA, Monaghan JJ. Smoothed particle hydrodynamics: theory and application to non-spherical stars. *Mon Not R Astron Soc*. 1977;181:375-389.
51. Liu WK, Jun S Zhang YF. Reproducing kernel particle methods. *Int J Numer Methods Fluids*. 1995;20(8-9):1081-1106.
52. Ai ZY, Liu CL, Jiang JP. Dynamic analysis of a vertically loaded rigid disc in a transversely isotropic multilayered half-space. *Meccanica*. 2016;51:1887-1895. doi:10.1007/s11012-015-0340-8
53. Nayroles B, Touzot G, Villon P. Generalizing the finite element method: diffuse approximation and diffuse elements. *Comput Mech*. 1992;10:307-318.
54. Powell MJD, The theory of radial basic function approximation. Advances in numerical analysis. Vol. II. 1992.
55. Babuška I, Rheinboldt WC. A-posteriori error estimates for the finite element method. *Int J Numer Methods Eng*. 1978;12:1597-1615. doi:10.1002/nme.1620121010
56. Chung H-J, Belytschko T. An error estimate in the EFG method. *Comput Mech*. 1998;21:91-100. doi:10.1007/s004660050286
57. Zienkiewicz OC, Zhu JZ. A simple error estimator and adaptive procedure for practical engineerng analysis. *Int J Numer Methods Eng*. 1987;24:337-357. doi:10.1002/nme.1620240206
58. Angulo A, Pozo LP, Perazzo F. A posteriori error estimator and an adaptive technique in meshless finite points method. *Eng Anal Boundary Elem*. 2009;33:1322-1338. doi:10.1016/j.enganabound.2009.06.004
59. Zienkiewicz OC, Zhu JZ. The superconvergent patch recovery and a posteriori error estimates. Part 2: error estimates and adaptivity. *Int J Numer Methods Eng*. 1992;33:1365-1382. doi:10.1002/nme.1620330703
60. Park SH, Kwon KC, Youn SK. A posteriori error estimates and an adaptive scheme of least-squares meshfree method. *International Journal for Numerical Methods in Engineering*, 58(8):1213-1250.
61. Kim HG, Atluri SN. Arbitrary placement of secondary nodes, and error control, in the meshless local Petrov-Galerkin (MLPG) method. *CMES—Comput Model Eng Sci*. 2000;1(3):11-32.
62. Chew WC, Jin JM, Michielssen E. Complex coordinate stretching as a generalized absorbing boundary condition. *Microwave Opt Technol Lett*. 1997;15:363-369.
63. Liu Gr, Karamanlidis D. Mesh free methods: moving beyond the finite element method. *Appl Mech Rev*. 2003;56(2):B17-B18.
64. Peirce WH. Numerical integration over the planar annulus. *J Soc Ind App Math*. 1957;5:66-73.
65. Peirce WH. Numerical integration over the spherical shell. *Math Tables and Other Aids to Computation*. 1957;11:244-249.
66. Schmitt DP. Acoustic multipole logging in transversely isotropic poroelastic formations. *J Acoust Soc Am*. 1989;86:2397-2421. doi:10.1121/1.398448

How to cite this article: Shaker K, Eskandari-Ghadi M, Mohammadi S. Meshless method for wave propagation in poroelastic transversely isotropic half-space with the use of perfectly matched layer. *Int J Numer Anal Methods Geomech*. 2024;1-29. https://doi.org/10.1002/nag.3797

APPENDIX A: MATRIX FORMS OF APPROXIMATIONS

The approximation of displacement vector at each computational point $\boldsymbol{x}$ is:

$$\hat{\boldsymbol{u}}^h(\boldsymbol{x}) = \sum_{k=1}^{n} \boldsymbol{\Phi}_k(\boldsymbol{x}, \boldsymbol{\xi})\widehat{\hat{\boldsymbol{u}}}_k = \boldsymbol{\Phi}(\boldsymbol{x}, \boldsymbol{\xi})\widehat{\hat{\boldsymbol{u}}} \tag{A.1}$$

If the stress tensor is written in the form of the following vector,

$$\boldsymbol{\sigma}_s^h(\boldsymbol{x}) = \left\{ \sigma_{11}^{s(h)}, \sigma_{22}^{s(h)}, \sigma_{33}^{s(h)}, \sigma_{12}^{s(h)}, \sigma_{23}^{s(h)}, \sigma_{13}^{s(h)} \right\} \tag{A.2}$$

then, it can be approximated as:

$$\boldsymbol{\sigma}_s^h(\boldsymbol{x}) = \boldsymbol{C}\bar{\boldsymbol{B}}(\boldsymbol{x})\widehat{\boldsymbol{u}} \tag{A.3}$$

where

$$\bar{\boldsymbol{B}}(\boldsymbol{x}) = [\bar{\boldsymbol{B}}_1(\boldsymbol{x}), \bar{\boldsymbol{B}}_2(\boldsymbol{x}), \dots, \bar{\boldsymbol{B}}_n(\boldsymbol{x})],$$

$$\bar{\boldsymbol{B}}_i(\boldsymbol{x}) = \begin{bmatrix} \frac{\partial \varphi_i}{\partial \tilde{x}_1} & 0 & 0 \\ 0 & \frac{\partial \varphi_i}{\partial \tilde{x}_2} & 0 \\ 0 & 0 & \frac{\partial \varphi_i}{\partial \tilde{x}_3} \\ \frac{\partial \varphi_i}{\partial \tilde{x}_2} & \frac{\partial \varphi_i}{\partial \tilde{x}_1} & 0 \\ 0 & \frac{\partial \varphi_i}{\partial \tilde{x}_3} & \frac{\partial \varphi_i}{\partial \tilde{x}_2} \\ \frac{\partial \varphi_i}{\partial \tilde{x}_3} & 0 & \frac{\partial \varphi_i}{\partial \tilde{x}_1} \end{bmatrix} = \begin{bmatrix} \frac{\partial \varphi_i}{\lambda_1 \partial x_1} & 0 & 0 \\ 0 & \frac{\partial \varphi_i}{\lambda_2 \partial x_2} & 0 \\ 0 & 0 & \frac{\partial \varphi_i}{\lambda_3 \partial x_3} \\ \frac{\partial \varphi_i}{\lambda_2 \partial x_2} & \frac{\partial \varphi_i}{\lambda_1 \partial x_1} & 0 \\ 0 & \frac{\partial \varphi_i}{\lambda_3 \partial x_3} & \frac{\partial \varphi_i}{\lambda_2 \partial x_2} \\ \frac{\partial \varphi_i}{\lambda_3 \partial x_3} & 0 & \frac{\partial \varphi_i}{\lambda_1 \partial x_1} \end{bmatrix}, \quad i = 1, 2, \dots, n \tag{A.4}$$

Thus, the traction vector at each computational point $\boldsymbol{x}$ is approximated as:

$$\boldsymbol{t}_s^h(\boldsymbol{x}) = \bar{\boldsymbol{N}}(\boldsymbol{x})\boldsymbol{\sigma}_s^h(\boldsymbol{x}) = \bar{\boldsymbol{N}}(\boldsymbol{x})\boldsymbol{C}\bar{\boldsymbol{B}}(\boldsymbol{x})\widehat{\boldsymbol{u}} \tag{A.5}$$

where

$$\bar{\boldsymbol{N}}(\boldsymbol{x}) = \begin{bmatrix} n_1 & 0 & 0 & n_2 & 0 & n_3 \\ 0 & n_2 & 0 & n_1 & 0 & n_3 \\ 0 & 0 & n_3 & 0 & n_2 & n_1 \end{bmatrix} \tag{A.6}$$

The fluid pressure at each computational point $\boldsymbol{x}$ is approximated as:

$$p^h(\boldsymbol{x}) = \boldsymbol{\varphi}(\boldsymbol{x})\widehat{\boldsymbol{p}} \tag{A.7}$$

Eventually, the fluid pressure gradient is calculated as follows:

$$\nabla p^h(\boldsymbol{x}) = \begin{Bmatrix} \frac{\partial \boldsymbol{\varphi}}{\partial \tilde{x}_1} \\ \frac{\partial \boldsymbol{\varphi}}{\partial \tilde{x}_2} \\ \frac{\partial \boldsymbol{\varphi}}{\partial \tilde{x}_3} \end{Bmatrix} \widehat{\boldsymbol{p}} = \begin{Bmatrix} \frac{\partial \boldsymbol{\varphi}}{\lambda_1 \partial x_1} \\ \frac{\partial \boldsymbol{\varphi}}{\lambda_2 \partial x_2} \\ \frac{\partial \boldsymbol{\varphi}}{\lambda_3 \partial x_3} \end{Bmatrix} \widehat{\boldsymbol{p}} = \bar{\boldsymbol{D}}(\boldsymbol{x})\widehat{\boldsymbol{p}} \tag{A.8}$$

Other values in the matrix form are as follows:

$$\bar{\boldsymbol{\alpha}} = \{\alpha_1, \alpha_2, \alpha_3, 0, 0, 0\}^T \tag{A.9}$$

$$\boldsymbol{n} = \{n_1, n_2, n_3\}^T \tag{A.10}$$

$$\boldsymbol{b} = \{b_1, b_2, b_3\}^T \tag{A.11}$$

$$\boldsymbol{w}(\boldsymbol{x}) = \begin{bmatrix} w_1 & 0 & 0 \\ 0 & w_2 & 0 \\ 0 & 0 & w_3 \end{bmatrix} \tag{A.12}$$

$$\bar{\boldsymbol{w}}(\boldsymbol{x}) = \left\{ \frac{\partial w_1}{\lambda_1 \partial x_1} \; \frac{\partial w_2}{\lambda_2 \partial x_2} \; \frac{\partial w_3}{\lambda_3 \partial x_3} \right\}^T \tag{A.13}$$

$$\bar{\boldsymbol{w}}_p(\boldsymbol{x}) = \left\{ \frac{\partial w_p}{\lambda_1 \partial x_1} \; \frac{\partial w_p}{\lambda_2 \partial x_2} \; \frac{\partial w_p}{\lambda_3 \partial x_3} \right\}^T \tag{A.14}$$

$$\boldsymbol{W}_p(\boldsymbol{x}) = \begin{bmatrix} \frac{\partial w_1}{\lambda_1 \partial x_1} & 0 & 0 \\ 0 & \frac{\partial w_2}{\lambda_2 \partial x_2} & 0 \\ 0 & 0 & \frac{\partial w_3}{\lambda_3 \partial x_3} \\ \frac{\partial w_1}{\lambda_2 \partial x_2} & \frac{\partial w_2}{\lambda_1 \partial x_1} & 0 \\ 0 & \frac{\partial w_2}{\lambda_3 \partial x_3} & \frac{\partial w_3}{\lambda_2 \partial x_2} \\ \frac{\partial w_1}{\lambda_3 \partial x_3} & 0 & \frac{\partial w_3}{\lambda_1 \partial x_1} \end{bmatrix} \tag{A.15}$$

Also, the relationship between the total stress, the effective stress on the solid skeleton, and the fluid pressure is:

$$\boldsymbol{\sigma}(\boldsymbol{x}) = \boldsymbol{\sigma}^s(\boldsymbol{x}) - p(\boldsymbol{x})\boldsymbol{\alpha} \tag{A.16}$$

It should be mentioned that $\widehat{\bullet}$ represents a nodal value, and $\widehat{\bar{\bullet}}$ is this value in the frequency domain.